FUNCTIONAL INTERACTIONS BETWEEN GYRI AND SULCI

by

FAN DENG

(Under the Direction of Tianming Liu)

ABSTRACT

This thesis focuses on functional interactions between gyri and sulci in the human brain. From the signal processing aspect, a data-driven signal decomposition framework was proposed and applied to infer meaningful low-frequency information from Blood Oxygenation Level Dependent (BOLD) time series from resting-state, task-based, and natural stimulus fMRI. From the data analysis aspect, a functional model of cortical gyri and sulci was proposed where we hypothesize that gyri are the global functional integration hubs and sulci are the local functional units. We examined and verified this functional model by structural and functional connectivity analysis on cortical landmarks of gyri and sulci, as well as whole brain correlation analysis performed on resting-state fMRI data. This functional model of gyri and sulci provides a novel perspective on the functional cortical architecture and offers a starting point for future elucidation of fine-scale functional mechanisms of the cerebral cortex.

INDEX WORDS: Functional brain architecture, fMRI, DTI, Connectivity, Signal decomposition, Functional image series analysis

FUNCTIONAL INTERACTIONS BETWEEN GYRI AND SULCI

by

FAN DENG

B.E., University of Science and Technology of China, China, 2009

A Thesis Submitted to the Graduate Faculty of The University of Georgia in Partial Fulfillment
of the Requirements for the Degree

MASTER OF SCIENCE

ATHENS, GEORGIA

2012

FUNCTIONAL INTERACTIONS BETWEEN GYRI AND SULCI

by

FAN DENG

Major Professor:	Tianming Liu
Committee:	Qun Zhao Suchendra M. Bhandarkar

Electronic Version Approved:

Maureen Grasso
Dean of the Graduate School
The University of Georgia
May 2012

DEDICATION

To

My Parents

ACKNOWLEDGEMENTS

This thesis and everything would not be possible without Dr. Tianming Liu’s three years’ industrious support, instruction, and guidance, which I cannot be more grateful for.

I would also like to thank Dr. Qun Zhao and Dr. Suchendra M. Bhandarkar for their excellent teaching and advisement.

My graduate life has been blessed because of my many friends. Even when things get tough, they never stop caring and supporting me.

TABLE OF CONTENTS

Page

CHAPTER

LIST OF TABLES

Page

LIST OF FIGURES

CHAPTER 1

INTRODUCTION

Functional Magnetic Resonance Imaging (fMRI) leverages the coupling between neuronal activity and hemodynamics in the human brain to obtain non-invasive localization and measurement of brain activity [1]. From a signal processing perspective, fMRI signal reflects the brain's hemodynamic responses to external stimuli or intrinsic oscillations of neuronal systems at multiple time scales [2]. From a neuroscience perspective, fMRI signal reflects the local field potential of synchronized neuron populations, simultaneous excitation and inhibition, modulatory inputs, or changes in neuronal synchrony [3]. Researchers use fMRI technology to image the human brain and record its real-time responses in a non-invasive way, making it possible to explore and study the functional mechanisms of the human brain.

Due to the vast complexity and variability of the structure and function of the cerebral cortex [4-9], studying the functional mechanisms of the human brain has been very challenging. As a consequence, the functional mechanisms of the human brain and their structural underpinnings remain largely unknown. From our perspective, a fundamental barrier to deciphering the functional mechanisms of the brain is the critical lack of joint representation and mapping of common structural and functional brain architectures, based on which functional mechanisms can be investigated and inferred. For instance, despite significant advancements of segmentation/parcellation of cortical gyri and sulci from structural MRI images in the past few decades [7, 10-15], the structural connection patterns and the functional roles of gyri and sulci still remain to be elucidated. Thanks to the recent advancements of modern in-vivo multimodal neuroimaging techniques, in particular, diffusion tensor imaging (DTI) [16] and fMRI [3, 17], we are now able to quantitatively measure the brain's axonal fiber wiring diagrams and functional activities with decent spatial and temporal resolutions [18-20]. The multimodal DTI/fMRI data offers unparalleled opportunities to investigating the structural architectures and functional mechanisms of the human brain [19-23]. Particularly, a joint representation and modeling approach of multimodal structural and functional neuroimaging data has demonstrated superior advantages in elucidating the structural/functional brain architectures [18-20, 23-25].

Using this joint representation and modeling approach, recent macro-scale neuroimaging and micro-scale bio-imaging studies revealed an interesting finding: axonal fiber terminations concentrate on gyri [26, 27]. That is, a dominant percentage of DTI-derived axonal fibers are connected to gyral regions, rather than sulcal regions. This finding has been replicated in DTI and Higher Angular Resolution Diffusion Imaging (HARDI) [28] data of human, chimpanzee, and macaque brains [26]. Furthermore, a joint representation of cortical gyral folding and axonal fiber connection patterns was applied to the analyses of a number of primate/human brains. The experimental results consistently demonstrate that gyral regions are connected by much denser axonal fibers than sulcal regions in the whole cerebral cortex in all brains we studied [26, 27], suggesting a common principle of structural brain architecture: gyri are the *structural connection hubs* of the cerebral cortex.

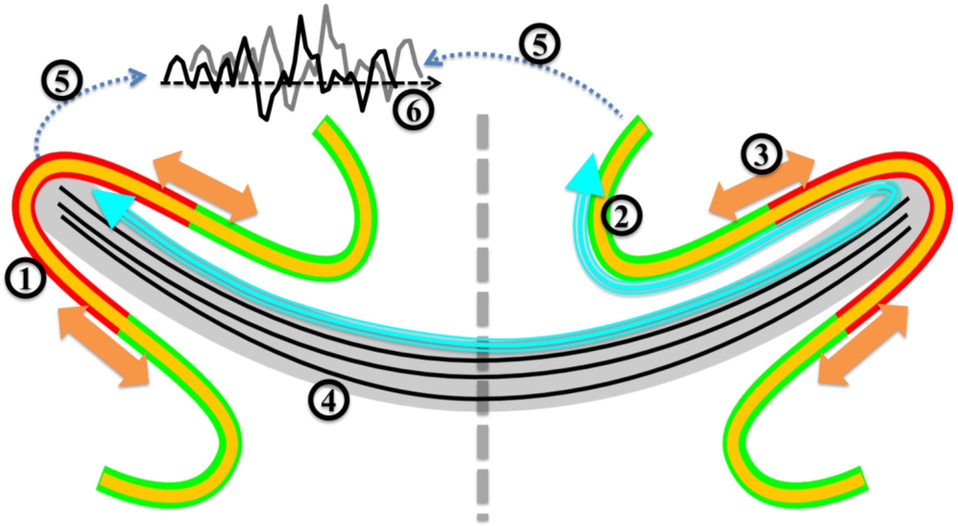

Fig. 1.1. Proposed functional model of cortical gyri and sulci. (1) A gyral region (red ribbon); (2) A sulcal region (green ribbon); (3) Sulci exchange information with neighboring regions via inter-column cortico-cortical axons (brown arrows); (4) Indirect communications are possible via dense axonal fibers (cyan arrow); (5) fMRI signals are extracted from cortical regions; and (6) Functional interactions measured by signal processing techniques.

Inspired by the above finding and the fact that axonal fibers are the structural substrates of functional connectivity [6], a functional model of the cerebral cortex is hypothesized: *gyri are the global functional integration hubs and sulci are the local functional units* [29]. Specifically, the hypothesized functional model of cortical gyri and sulci is illustrated in Fig. 1.1. The main idea here is that gyral regions are the functional integration hubs that exchange information between distant gyral regions via dense axonal fibers (black curves in Fig. 1.1), while sulcal regions communicate directly with their neighboring gyri through inter-column cortico-cortical axons (brown arrows in Fig. 1.1, [30]) and communicate indirectly with remote cortical regions via the gyri hubs and their dense axonal connections (cyan arrow). It should be noted that the local inter-column cortico-cortical axons cannot be imaged and revealed by current in-vivo DTI techniques [16], but they do play important roles in inter-column neural communications [5, 30].

Once the functional units are identified, signal processing and analysis techniques play important roles in studying functional interactions in the human brain (6 in Fig. 1.1). In the literature, a great amount of effort has been devoted into this area, e.g., the generalized linear models (GLM) [31], wavelet algorithms [32, 33], Markov random field (MRF) models [34], mixture models [35], autoregressive spatial models [36], Bayesian approaches [37], and independent component analysis (ICA) [38, 39]. Though these model-driven approaches have their own advantages in various applications [31-39], the characteristics of non-linearity and composition of signal components at multiple time scales in fMRI Blood Oxygenation Level Dependent (BOLD) signals present significant challenges to the inference of meaningful information from fMRI BOLD data. In particular, it was reported that neuronal networks in the brain demonstrate a variety of oscillatory bands covering frequencies from approximately 0.01 Hz to 500 Hz [2], which means that fMRI BOLD signal has complex composition of signals at a wide range of time scales in nature, laying down the fundamental need for data-driven, multi-scale decomposition methods of fMRI BOLD signal. In addition, fMRI BOLD signal might be subject to physiological motion effect or non-neuronal noise [1, 3]. As such, non-linearity and low signal-to-noise ratio are common in fMRI time series data [1, 3], which further entails the decomposition of fMRI BOLD signal into meaningful components and random noise residue.

This thesis focuses on discovering and further understanding the functional interactions between gyri and sulci in the human brain from both aspects. We propose in Chapter 2 a data-driven signal decomposition framework to decompose fMRI BOLD time series data into model-free components [40]. The framework was applied to infer meaningful low-frequency information from BOLD signals from resting-state fMRI, task-based fMRI, and natural stimulus fMRI. In Chapter 3 we hypothesize a functional model at the gyri/sulci level of the human brain and verify it using a joint representation and modeling approach with joint DTI/fMRI data [29]. This functional model of gyri and sulci provides a novel perspective on the functional cortical architecture and offers a starting point for future elucidation of fine-scale functional mechanisms of the cerebral cortex.

CHAPTER 2

EMPIRICAL MEAN CURVE DECOMPOSITION

2.1 Data-driven fMRI Signal Analysis

In the signal processing community, empirical mode decomposition (EMD) [41-43] has been recognized as an effective data-driven signal decomposition approach and has been widely used in multi-scale signal analysis [44]. The EMD algorithm was initially proposed to study ocean waves [41], and has been applied in solving biomedical signal processing problems [45-49], e.g., in [45] for field potential recording analysis and in [48] for task-based fMRI activation detection. In brief, EMD extracts intrinsic mode functions (IMFs) by iteratively removing mean curves from the input time series (or the residue in subsequent iterations) until the residue becomes an IMF. EMD features a unique decomposition scheme that the IMFs are derived from the time series data directly without prior domain knowledge. Therefore, it is adaptive, in contrast to wavelet or Fourier analysis where the basis functions are predefined in advance.

The data-driven manner of decomposing time series makes EMD a powerful tool in analyzing many types of time series data. In spite of EMD's superiority over many model-based decomposition methods, direct applications of EMD in fMRI BOLD signal analysis might not be appropriate for several reasons. The major issue is the strict constraints of IMF which forces all components extracted by EMD to be (1) narrow-band limited; and (2) with zero local mean. These constraints ease theoretical analysis and provide a fairly simplified model of the components of prospect. In fMRI time series analysis, as well as many other biomedical applications, however, the ultimate goal of signal decomposition is to reconstruct the intrinsic, biologically meaningful components rather than mathematically defined ones. In particular, EMD extracts higher-frequency components first, employing a finer-to-coarser scheme. In fMRI time series analysis, the major noise source is of high-frequency while low-frequency global drifting are typically overcome by detrend algorithms [50]. Accordingly, the EMD decomposition results are unstable due to its unavoidable error in extracting the highest-frequency component. Thus, the error accumulates rapidly in subsequent iterations. When it reaches the most desirable scale in the low-frequency bands [1, 17], the component might have been deteriorated by the accumulated error.

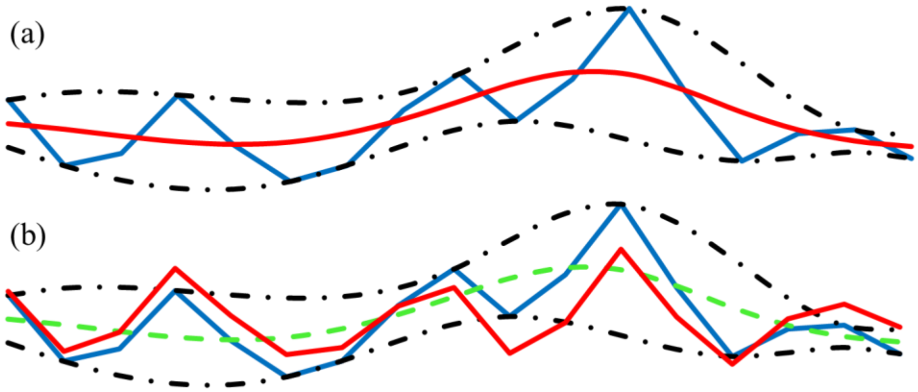

Fig. 2.1. A conceptual comparison between EMCD (a) and EMD (b). For both (a) and (b) the blue curve is the original time series; its superior and inferior envelopes are depicted as dark dashed curves. (a) Red curve: extracted mean curve component in EMCD. (b) Red curve: extracted IMF in EMD. EMCD makes use of extrema optimization to improve the decomposition, which does not exist in EMD.

In response to the major limitations of applying EMD in fMRI time series analysis and in the meanwhile inspired by this data-driven signal decomposition methodology, a novel multi-scale, iterative signal decomposition framework named Empirical Mean Curve Decomposition (EMCD) is proposed to deal with the above issues in fMRI signal decomposition. The EMCD algorithm calculates both the superior and inferior envelopes in each iteration of signal decomposition (Fig. 2.1), applies a scale control algorithm to optimize the envelopes, and extracts the mean curve by averaging the superior and inferior envelopes. This algorithm is iteratively applied on the residue signal, which is the subtraction of the extracted mean curve from the original signal. Sections 2.2 and 2.3 will cover the details of the algorithm and framework.

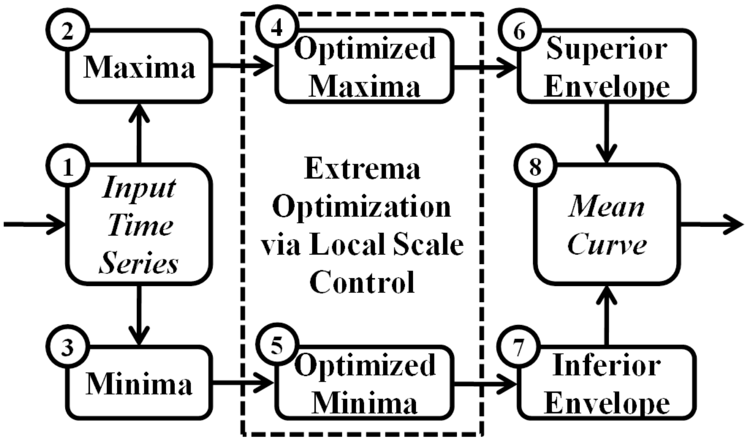

Fig. 2.2. A general flowchart of the algorithm.

2.2 Decomposition Basics

A general flowchart of the EMCD decomposition algorithm is shown in Fig. 2.2. The algorithm decomposes a time series in a multi-scale, data-driven manner. Briefly, the maxima (Step 2) and minima (Step 3) are extracted from the input time series (Step 1). They are optimized (Step 4, Step 5) by a local scale control algorithm and are interpolated to form superior envelope (Step 6) and inferior envelope (Step 7), respectively. The local scale control algorithm moderately controls the scale to which the time series is decomposed. The mean curve (Step 8) as the output is calculated by averaging both envelopes. This decomposition algorithm is iteratively applied to the input time series (in its first iteration) and the residues (in the following iterations).

Let x[n], n=1, …, N be an N-element time series which we will refer to as x[n]. (p_i, x[p_i]), i=1, …, N_p is the maxima series of x[n], where p_i is the time index and N_p is the number of maxima; (q_i, x[q_i]), i=1, …, N_q is the minima series of x[n], where q_i is the time index and N_q is the number of minima; B[(x_i, y_i), x_0] is the widely used B-spline interpolation function which interpolates the input series (x_i, y_i) at time point x_0.

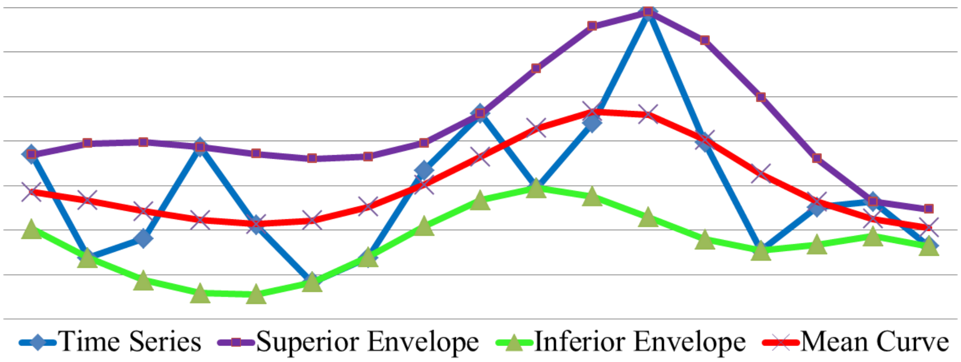

Fig. 2.3. An example of superior/inferior envelopes and mean curve.

Superior Envelope

The superior envelope of a time series is the upper trend curve that passes through all of its maxima (purple curve in Fig. 2.3). The B-spline interpolation is used to interpolate the maxima:

Equation 2.1 $$x^{\sup}[n] = B[(p_i, x[p_i]), x[n]], n = 1,..., N$$

Inferior Envelope

Similarly, the inferior envelope of a time series is the lower trend curve that passes through all of its minima (green curve in Fig. 2.3):

Equation 2.2 $$x^{\inf}[n] = B[(q_i, x[q_i]), x[n]], n = 1,..., N$$

Mean Curve

The mean curve of a time series is the average of its superior and inferior envelopes (red curve in Fig. 2.3) representing the global trend:

Equation 2.3 $$x^{mean}[n] = (x^{\sup}[n] + x^{\inf}[n])/2, n = 1,..., N$$

The notations introduced above are illustrated in Fig. 2.3.

Mode

The mode of a time series is defined as the average of its number of maxima N_p and minima N_q:

Equation 2.4 $$M(x[n]) = (N_p + N_q)/2$$

Empirical Wave Form

The fact that the mean curve is determined by the extrema provides a new way to model time series. Here we introduce the concept of Empirical Wave Form (EWF). A EWF is a series of alternating maxima and minima. A simplified EWF is defined as follows:

Equation 2.5 $$EWF(x[n]) = \{(p_i, x[p_i]), (q_i, x[q_i])\}$$

Then we can use a EWF to represent a mean curve, while its mode, M(x[n]) (Equation 2.4), characterizes this EWF. In principle, one complete sine wave cycle has one maximum and one minimum, contributing exactly one to its mode. Hence the mode of a EWF behaves like the number of complete cycles in traditional Fourier analysis. We derive the *empirical period* for the above EWF as:

Equation 2.6 $$T_{EWF} = N / M(x[n])$$

while the *empirical frequency* is given by:

Equation 2.7 $$f_{EWF} = M(x[n]) / N$$

These concepts are listed in Table 2.1 (next page) in conjunction with their corresponding terms in traditional Fourier analysis for comparison.

It should be noted that empirical period and empirical frequency are temporal estimations over the entire time series rather than the exact model parameters as in traditional Fourier analysis. This relaxation of conditions improves the descriptive abilities such that a wider class of signals from different oscillatory sources can be modeled, e.g., neurons and brain regions, whose signals are similar to (in the sense of their shapes), but not the same as, sine waves. As a comparison, the Fourier analysis decomposes this type of time series into a set of sine waves at different frequencies, and the wavelet transform decomposes them into a set of wavelets at multiple frequencies and different temporal locations.

Table 2.1. COMPARISON OF CONCEPTS

Concept	Empirical Wave Form	Fourier Analysis
Form	$x[n]$, $(p_i, x[p_i])$, $(q_j, x[q_j])$	$y[n]$, $\sin(\omega n)$
Period	$N/M(x[n])$	$2\pi/\omega$
Frequency	$M(x[n])/N$	$\omega/2\pi$

Theoretically, any time series can be modeled as a EWF once we have extracted the extrema, so is any continuous range of an existing time series. Considering the local properties of the time series, we define *local scale* as the local period of a cycle. Here by "cycle" we refer to the range of a pair of adjacent maximum and minimum. For a time series with multiple components in the form of riding waves, the local scale descriptor may vary largely at different cycles within the time series. In order to effectively model the time series, we process the time series in its empirical wave form to recover singular EWF components without riding waves, in which a *local scale control* algorithm is employed to optimize the EWF. We refer to the recovered singular EWF components as "pure" EWFs.

In short, the goal of the proposed EMCD algorithm is to decompose the time series at different scale levels, yielding a composition of pure EWFs. In that sense, these pure EWFs are the basis functions in EMCD, compared to the sine waves in Fourier analysis and the wavelets in wavelet transforms. These empirical basis functions, however, require no prior knowledge of the signal model and are thus purely data-driven. Orthogonality, therefore, is not guaranteed.

2.3 Decomposition Framework

The main procedure of EMCD is the iterative decomposition process, which is applied on the input time series to produce the mean curve as the output.

Extrema Extraction

The algorithm extracts both maxima and minima as the initial step of the iterative process.

Local Scale Control

This step of the algorithm controls the local scale of the extrema. Recall that by “local scale” we refer to the length of period of a certain cycle. Furthermore, as cycles are determined by extrema, we control the local scale by inserting extrema time points, since the extracted extrema are data-dependent and are not to be modified. Basically, the local scale controls how much alike we want the extracted mean curve and the input time series to be, since the reconstruction of envelopes depends solely on the extracted extrema. If two extrema are too far away, it may be infeasible to recover the true envelope.

The local scale control procedure applies to both maxima and minima with the same method. Taking maxima as an example, for each pair of adjacent maxima, the number of time points they are apart is calculated as the *distance* of the pair. By definition, this distance is the local scale. If it is larger than a pre-selected scale threshold, we need to insert a certain number of new nodes as the “interpolated” maxima between the two real ones. This process controls the local scale at each maximum.

Specifically, suppose the maxima pair, (x[u], x[v]), u<v, are currently in consideration. Its distance is calculated as:

Equation 2.8 $$D = v - u + 1$$

Let S be the scale threshold. We calculate the number of new nodes to insert and their locations as:

Equation 2.9 $$N_{new} = \lceil D / S \rceil - 1$$

Unlike the indices u and v, the locations L[n] need not to be rounded to integers since those inserted nodes will be used only in the interpolation procedure. Meanwhile, the amplitudes at these nodes are derived from the following Gaussian model:

Equation 2.10 $$G[t] = \begin{cases} E[v](e^{-1/2\sigma^2} - e^{-t^2/2\sigma^2}) & t \geq 0 \\ E[u](e^{-1/2\sigma^2} - e^{-t^2/2\sigma^2}) & t < 0 \end{cases}$$

Equation 2.11 $$\Delta[L[n]] = G[2\frac{L[n] - (v+u)/2}{v-u}]$$

where E[u] is the estimate of the amplitude difference at maximum x[u] between the expected mean curve and the original time series; E[v] is the estimated amplitude difference at maximum x[v]; σ is the scaling parameter of the Gaussian model which controls the shape; G[t] is the Gaussian model; the estimated difference in amplitude at L[n] between the expected mean curve and the original time series is given by Δ[L[n]]. The amplitude difference estimates can be derived from smoothing the time series. Therefore, the amplitude for the n^{th} interpolated node is:

Equation 2.12 $$A[n] = x[L[n]] + \Delta[L[n]]$$

Interpolation

Once we have the optimized extrema from the previous step, B-spline interpolation is used to obtain the superior envelope and inferior envelope. The output mean curve is obtained by averaging both envelopes.

The Decomposition Framework

Having obtained a mean curve, C, we employ a practical strategy to determine whether this is a valid pure EWF. The extracted mean curve is simply decomposed one more time into C' and residue R' (C=C'+R'). C is considered as a valid pure EWF only if either of the following criteria is *not* met:

- The difference between M(C') and M(R') is larger than a given threshold;
- The variance values of both C' and R' are larger than a given threshold.

The first criterion confirms that a riding wave exists in C; and the second ensures that both C' and R' are statistically non-trivial. If either of the two criteria is not met, C is a valid pure EWF or useless residue; otherwise, we continue the test using C'. Depending on the complexity of the data, this process might be repeated a few times until the riding wave diminishes, which must happen because of the nature of the decomposition method.

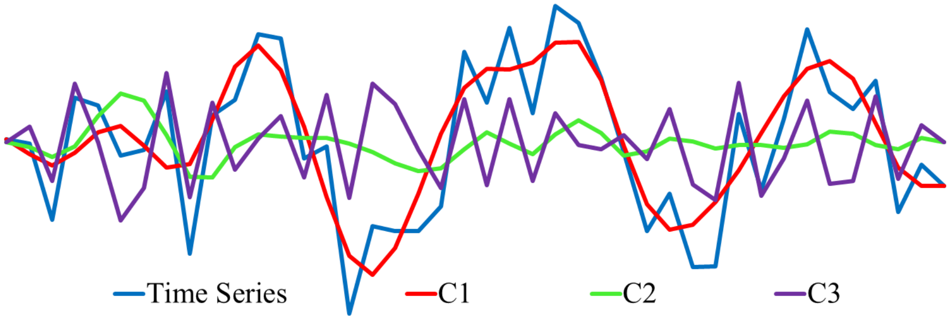

Fig. 2.4. A full EMCD decomposition of an fMRI BOLD time series into three EWFs. C1 and C2 are the first and second components and C3 is the residue.

After each iteration, the residue is also tested for variance conditions. If the variance of the residue after an iteration is too low, the algorithm terminates to avoid generating trivial components. Therefore, the input time series, X[n], is decomposed into a number of pure EWFs (EMCD components) and a residue (which is a EWF as well). The number of extracted pure EWFs depends on the data and the local scale threshold. In summary, we have:

Equation 2.13 $$x[n] = \sum_{i=1}^{N_{EWF}+1} C[i]$$

where N_{EWF} is the number of extracted pure EWFs determined by the data; the residue is rewritten as $C[N_{EWF}+1]$. The original time series is merely the addition of all the decomposed EWFs. As an example, depicted in Fig. 2.4 is a decomposition of an fMRI BOLD time series.

It should be noted that the largest scale (the first component) is data-dependent. A further decomposition of the first component yields even larger scale components.

In comparison with EMD, EMCD focuses on improving the extraction of components at a low frequency or coarser scale. This is especially useful in fMRI analysis where the major noise source is of higher frequency, which typically forms the residue in EMCD results.

2.4 Experiment Data

Resting state fMRI data

Resting state fMRI data were acquired in a 3T HDx GE MRI system (GE Healthcare, Milwaukee, WI) with dimensionality 128*128*60*100, spatial resolution 2mm*2mm*2mm, TR 5s, TE 25ms, and flip angle 90 degrees. Standard pre-processing procedures were applied, including brain skull removal, motion correction, spatial smoothing, temporal pre-whitening, slice time correction, and global drift removal [50, 51]. DTI data were acquired using the same spatial resolution as that of resting state data, with TR 15.5s, TE 89.5ms, 30 DWI gradient directions, and 3 B0 volumes. Standard pre-processing procedures were applied, including brain skull removal, motion correction, and eddy current correction. Fiber tracking was performed using MedINRIA [32] (FA threshold: 0.2; minimum fiber length: 20; sampled by four). We used DTI as the standard space by registering resting state data to the DTI space [50, 52, 53].

Task-based fMRI data

Task-based fMRI is very useful in localizing function regions of interests (ROIs) in the human brain and is widely used in the brain imaging community [1, 3, 31]. In this experiment, we decomposed the task-based fMRI BOLD time series [54] using the proposed EMCD framework, and compared the decomposed components with the result provided by FSL FEAT [55], which is widely used in the community. The pre-processing steps of task-based fMRI BOLD signals were based on published methods in [52, 56] and the auditory task-based fMRI data [54] was used in the experiments.

Natural stimulus fMRI data

The datasets we used were reported in [54]. Briefly, natural stimulus fMRI data was scanned in a news-watching session. The news multimedia was selected from the TRECVID 2005 dataset [57]. Low-level audio/video features were extracted [54], including visual motion saliency [58] and audio signal energy. Twenty-nine brain regions from the vision, auditory, language, and working memory networks were mapped via task-based fMRI [54], and the natural stimulus fMRI signals scanned in separate sessions were extracted from these functional brain regions [54]. The preprocessing steps of these natural stimulus fMRI signals are referred the published methods in [52, 54].

2.5 Results

EMCD on synthesized time series

In this experiment, we aim to evaluate EMCD on signal recovery in the presence of noise, and compare it with EMD and wavelet transform, both of which are well-established multi-scale signal decomposition methods.

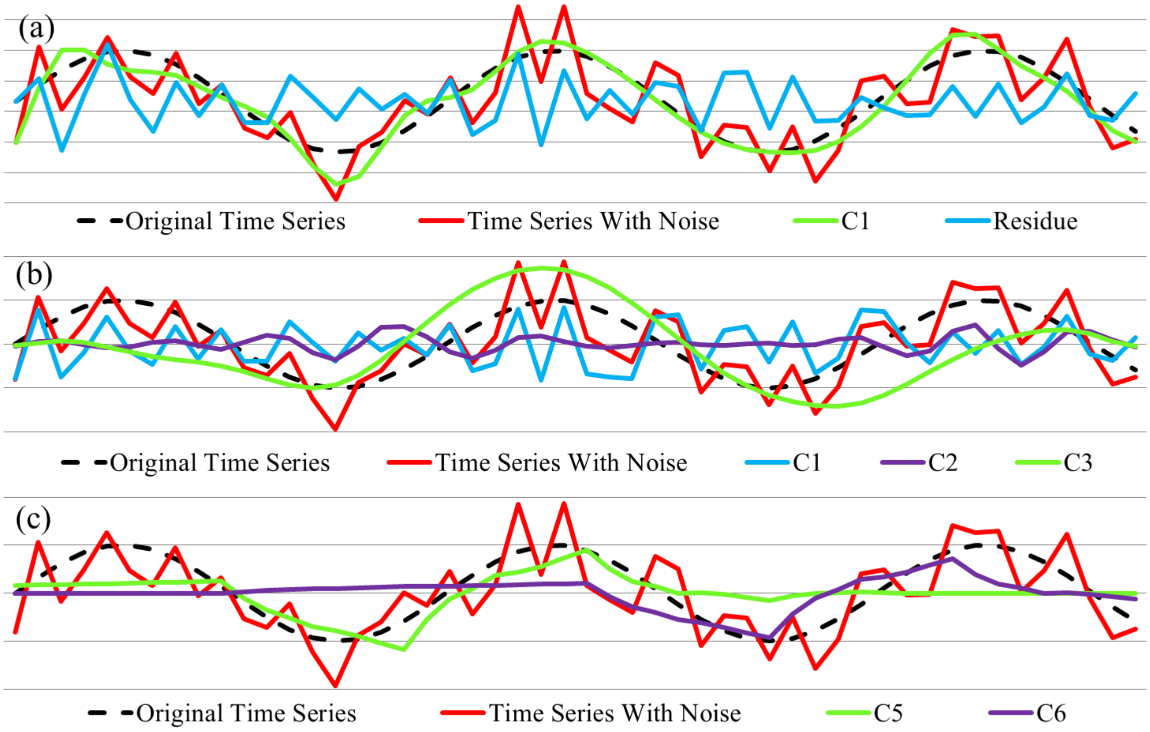

Fig. 2.5. Comparisons of time series decomposition on synthesized time series. (a) EMCD results; (b) EMD results; (c) results from Daubechies wavelet transform. Notice that we only plotted the non-trivial components. In all subfigures, dark dashed curves refer to the original time series (the sine wave); red: time series with random noise; green: the most representative component as C1 from EMCD, C3 from EMD and C5 from wavelet transform.

The synthesized time series was decomposed using EMCD, EMD, and Daubechies wavelet transform as shown in Fig. 2.5a-c, respectively. The dark dashed curve is the original time series without noise, i.e. sin(n/3). The synthesized time series with noise is colored in red. Note that only non-trivial components are plotted in the figure. The shown components include C_1 and the residue from the proposed EMCD framework (Fig. 2.5a), C_1 and C_3 from EMD (Fig. 2.5b), and C_5 and C_6 from the wavelet transform (Fig. 2.5c).

It is evident that the proposed EMCD decomposition component C_1 matches the benchmark sine wave with high accuracy. In contrast, the result of EMD suffers from the algorithm's instability to noise because it extracts high frequency components first and accumulates error quickly in subsequent sifting processes, as demonstrated in Fig. 2.5b. In Fig. 2.5c, it is evident that the wavelet transform can hardly recover the original shape since it is model-driven and the basis functions can hardly match the signal shapes in the data without prior information. All it generates are linear combinations of its basis functions, as shown in Fig. 2.5c.

The choice to select the first EMCD component as the representing one is empirical rather than theoretically supported at current stage. In this synthesized time series experiment, the first component has the right scale that is comparable to that of the sine wave model. In other applications, e.g., natural stimulus fMRI, choosing the right scale becomes non-trivial when the external stimulus feature curves have a much higher sampling rate than that of fMRI time series. To ensure comparisons between components at the same scale, further analysis is essential.

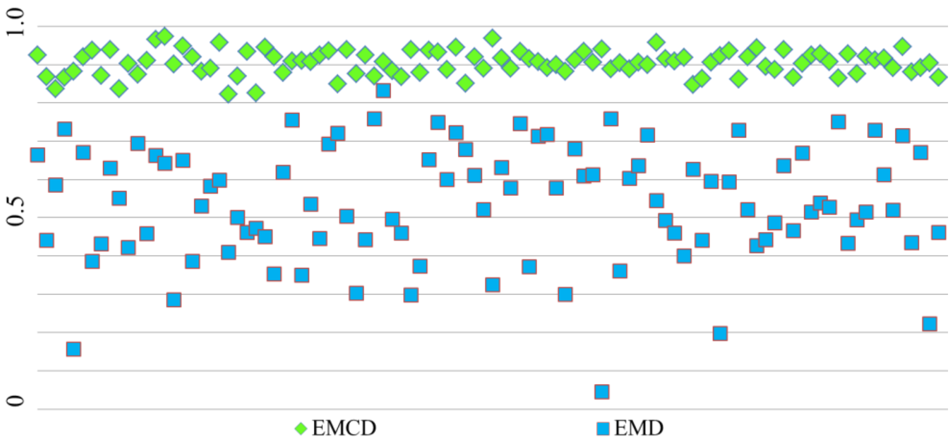

Fig. 2.6. Comparison between EMCD and EMD in measuring the Pearson correlation of 100 synthesized time series with random noise and the original sine wave.

Quantitatively, we compared EMCD and EMD in measuring Pearson correlation of 100 synthesized time series with random noise and the original sine wave. The results are shown in Fig. 2.6, from which we can see that EMCD achieves substantially better correlation results consistently. Specifically, the mean and variance are 0.904 and 0.001 for EMCD results; and

0.537 and 0.023 for EMD results. The wavelet method was not included in this correlation analysis experiment since it is model-driven, which could bias the comparison results.

To summarize this section, both qualitative and quantitative evaluations using synthesized time series signals with ground-truth demonstrated that the proposed EMCD framework has superior performance in extracting meaningful true components from contaminated signals.

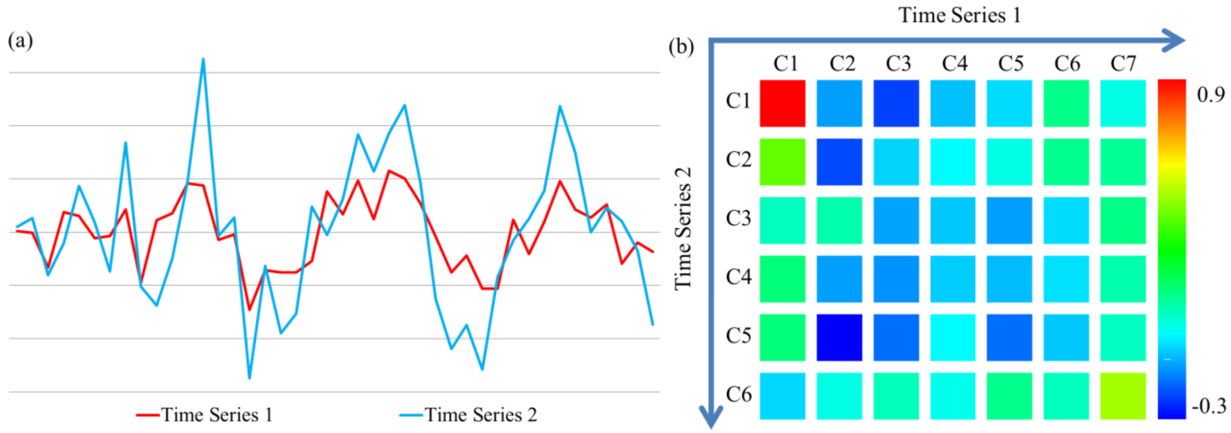

Fig. 2.7. Correlation structure between two time series. (a) The time series; (b) the correlation structure matrix. There are six components and a residue for time series 1, and five components and a residue for time series 2. The color bar is on the right.

EMCD in Resting State fMRI Analysis

In this experiment, we applied the EMCD framework in resting state fMRI [17, 50, 59-61] analysis to discover the multi-scale correlation structure as well as the spectral characteristics of EWFs in the resting state frequency bands.

With the proposed decomposition framework, we are able to measure the EWFs correlation structure between two fMRI time series in a multi-scale manner. Suppose we have two resting state fMRI time series X and Y. They are decomposed using EMCD as:

Equation 2.14 $$X = \sum_{m=1}^{K_X+1} C_m^X$$

Equation 2.15 $$Y = \sum_{n=1}^{K_Y+1} C_n^Y$$

Then, their correlation structure is given in the form of a matrix (P_C stands for Pearson correlation):

Equation 2.16 $$[C_{orr}^{m,n}] = P_C(C_m^X, C_n^Y)$$

Fig. 2.7 shows an example of the EWF's correlation structure between two resting state fMRI time series. Elements colored in red or green indicate stronger correlation. As we can see from Fig. 2.7, this matrix reveals the scales the two time series are most correlated at. This capability has wide applications in measuring the functional connectivity between resting state fMRI signals at different frequencies [44] in the future.

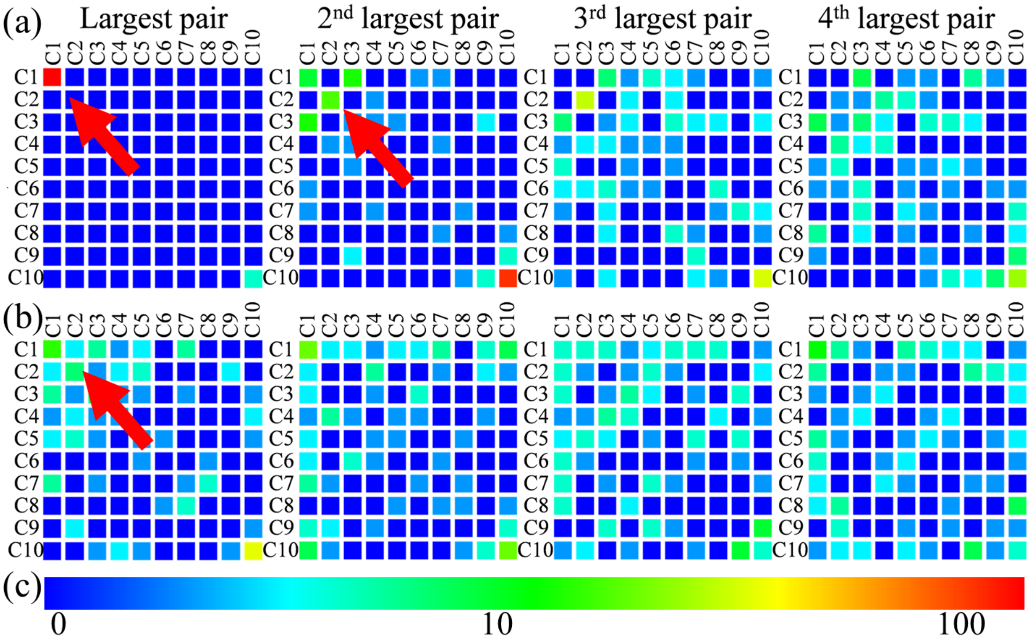

Fig. 2.8. Corresponding correlation pair distributions in the correlation structures. The color bar (logarithm scale) is at bottom. (a) Time series pairs with white matter fiber connections; (b) Time series pairs without white matter fiber connections; (c) The logarithmic color bar representing the number of time series.

We conducted additional experiments to evaluate this multi-band correlation structure analysis on more resting state fMRI data as shown in Fig. 2.8. Two groups of time series pairs were selected. Group A contains 100 randomly selected time series pairs from voxels with strong white matter fiber connections derived from DTI data [51], while group B contains 100 randomly selected time series pairs from voxels without white matter fiber connections. The functional connectivity strengths were originally measured by Pearson correlation [51]. Here, for each time series pair, we estimated its multi-band functional correlation structure using EMCD. Taken column 2 in Fig. 2.8 as an example, the colors of the elements in the matrices indicate the numbers of cases out of 100 that have their second largest functional correlation values at the corresponding EMCD component pairs. Notice that the extracted EMCD components may be more than ten, which is the dimension of the matrix. We merged all elements beyond that limit to the right-bottom one within the matrix. As shown in Fig. 2.8, the EMCD revealed interesting characteristics of the two types of time series pairs: (1) for time series from voxels with strong DTI-derived white matter fiber connections, more than 90% of its largest functional correlation values resides in C_1-C_1 pair (left panel in Fig. 2.8), while the largest functional correlation values of time series from voxels without white matter fiber connections have a sparse distribution as indicated by the red arrows in Fig. 2.8b; (2) the distributions of the 3rd and 4th largest pairs are alike in both time series pairs. We interpret that the observed differences between the two types of time series pairs in Fig. 2.8 might originate from the intrinsic characteristics of the time series. As of the pairs with structural fiber connections, the time series pairs in group A are strongly correlated and the correlation structures concentrate on a few scales. The time series pairs in group B, however, are not associated with fiber connections and are thus weakly correlated, the correlation structures of which are therefore displaying a sparsely distributed pattern.

This result is quite reasonable, considering the close relationship between structural and functional connectivity in the human brain [6, 18]. Thus, given the lack of ground-truth data in fMRI, this cross-validation result based on independent DTI-derived structural connection patterns strongly support the biological meanings of our EMCD framework and the decomposed EWFs.

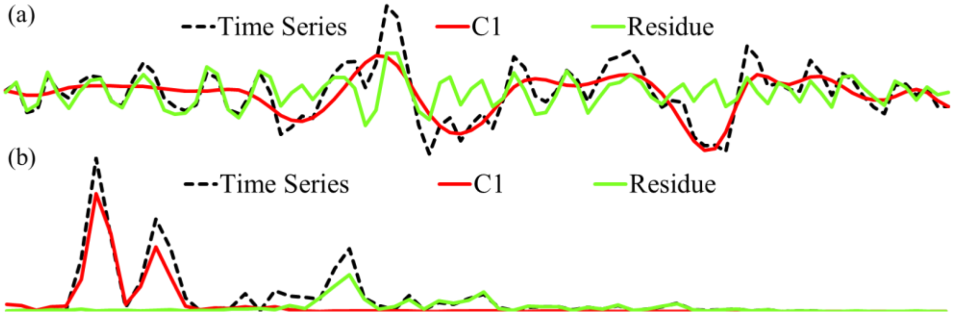

Fig. 2.9. Decomposition of a resting state fMRI time series (a) and Fourier spectrum plots (b). In (a) only C1 and the residue are plotted.

In comparison with the traditional low-pass filters commonly used in the signal processing community, EMCD naturally forms a band-pass filter whose spectrum response is non-linear and data-driven. An example is shown in Fig. 2.9, from which we can see that the extracted different EWFs are separated in the Fourier frequency domain. This figure provides an intuition of how EMCD works in decomposing resting state fMRI signals in the frequency domain.

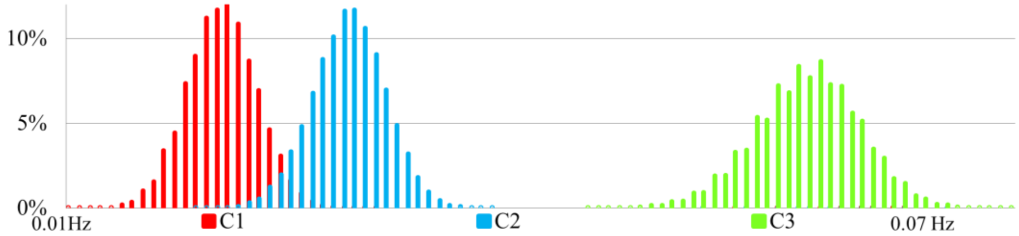

Fig. 2.10. Empirical frequency statistics of resting state fMRI data. Horizontal axis refers to the empirical frequency; vertical axis refers to the percentage of time series at the corresponding empirical frequency.

With the notation of EWF, we can calculate the empirical frequency for each extracted EWF component. Fig. 2.10 shows the statistics of empirical frequency distributions of resting state time series from grey matter voxels in one human brain as an example. Specifically, the resting state fMRI time series were decomposed into three EWFs. In Fig. 2.10, the horizontal axis refers to the empirical frequency, and the vertical axis refers to the percentage of time series at the corresponding empirical frequency. For each EWF component, the distribution of empirical frequency shows a Gaussian-like pattern. The mean empirical frequency of C_1 is 0.020 Hz; for C_2 it is 0.028 Hz; and for C_3 it is 0.057 Hz. We analyzed other 8 brains with resting state fMRI data and found similar patterns. These frequency distributions are quite consistent with the reports in the resting state fMRI literature [3, 17].

Importantly, it is also evident in Fig. 2.10 that the variation of frequency distributions of resting state fMRI signals across different brains is remarkable, as demonstrated by the standard deviations of the three Gaussian distributions. This variation imposes significant difficulty in selecting the best upper and lower band-limits when designing traditional low-pass or band-pass filters for decomposing the fMRI signals. In contrast, our data-driven EMCD decomposition method is adaptive to data itself and provides superior flexibility in fMRI signal decomposition, which is the major advantage of the proposed EMCD framework.

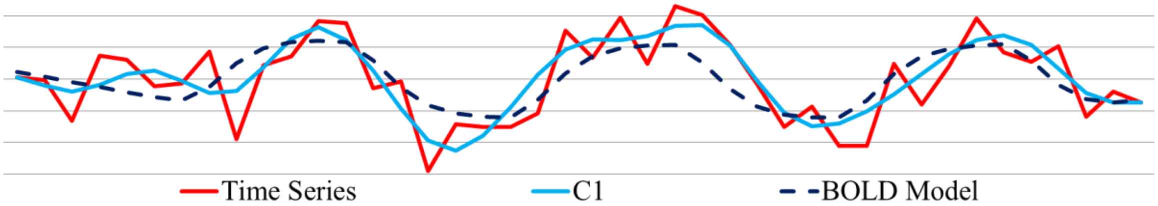

Fig. 2.11. The decomposition framework applied to task-based fMRI data. The red curve is the original fMRI time series, while the blue one is the first EMCD component and the black dashed curve is the BOLD model fit by FSL FEAT.

EMCD in Task-based fMRI Analysis

Fig. 2.11 shows an example of EMCD decomposition of task-based fMRI time series. We can see that the first EMCD component C_1 closely matches the FEAT BOLD model, which is a convolution of the Hemodynamic Response Function (HRF) with a linear combination of explanatory variables such as block-based paradigm stimuli and motion factors.

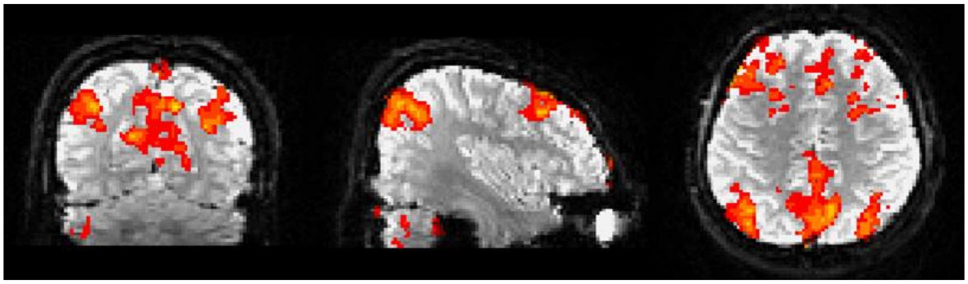

Fig. 2.12. FSL FEAT activation results in an auditory task-based fMRI dataset.

We compared the correlations between the FEAT BOLD model and the signals decomposed by EMCD, EMD, and the original fMRI signal, respectively. We randomly selected 100 fMRI time series from activated voxels in the auditory task-based fMRI [54] and the other 100 time series from non-activated voxels. The activation map was detected by the FSL FEAT as shown in Fig. 2.12.

For EMCD, we calculated the Pearson correlation between the first EMCD component and the BOLD model; for EMD, we calculated the Pearson correlation between each of the components and the BOLD model, and selected the most significant value; for the original fMRI signal, we simply calculated the Pearson correlation value between the raw fMRI time series and the BOLD model. The results are shown in Fig. 2.13 (next page). In Fig. 2.13a, the mean and variance are 0.755 and 0.004 for EMCD, 0.491 and 0.037 for EMD, and 0.636 and 0.002 for original fMRI signal. It is evident that the first EWF component decomposed by the EMCD framework has the highest correlation to the stimulus curve, suggesting that the lower frequency component in fMRI signal is the biologically relevant signal that is of interest to us and the EMCD approach is able to effectively extract this meaningful component. In contrast, the original fMRI signal might be contaminated or influenced by other irrelevant components of higher frequencies, and the EMD method extracts irrelevant higher frequency signal components first and the error could accumulate rapidly in subsequent iterations when it starts the extractions of the biologically meaningful components.

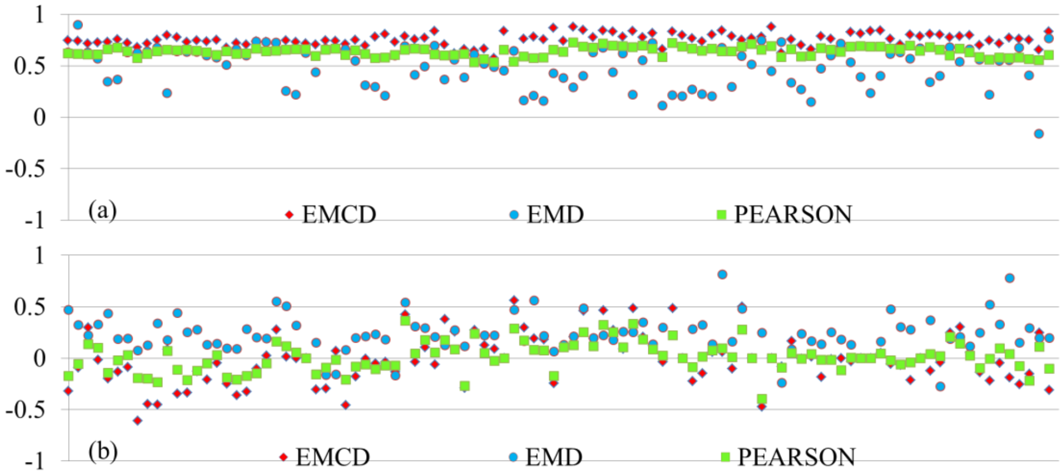

Fig. 2.13. Correlations between the FSL FEAT BOLD model and the EMCD components, the EMD components and raw fMRI signals. The numbers on the left refer to the correlation values. (a) Results for 100 time series from randomly selected activated voxels in auditory task-based fMRI dataset; (b) Results for 100 time series from randomly selected non-activated voxels in the same dataset.

In Fig. 2.13b where 100 fMRI time series from non-activated voxels are shown, the means and variances of correlations are -0.014 and 0.057 for EMCD, 0.217 and 0.033 for EMD, and 0.008 and 0.020 for original fMRI signal, respectively. This result suggests that when there is no correlation between the fMRI signal and stimulus curve, EMCD, EMD and Pearson correlations have similar outcomes. It can be seen that the specificity of the EMCD framework in extracting relevant signal components is also very good, given its substantially better sensitivity than the EMD and Pearson correlation methods.

The experimental results in this section demonstrated that the proposed EMCD decomposition framework substantially better recovered the intrinsic BOLD activity embedded in the fMRI time series data that is induced by the block-based external stimulus than the EMD and Pearson correlation methods. Considering that the external stimulus curve of block-based paradigm is widely regarded as the benchmark data, the results based on task-based fMRI data partially validated the effectiveness and accuracy of the proposed EMCD framework in extracting biologically relevant signal components.

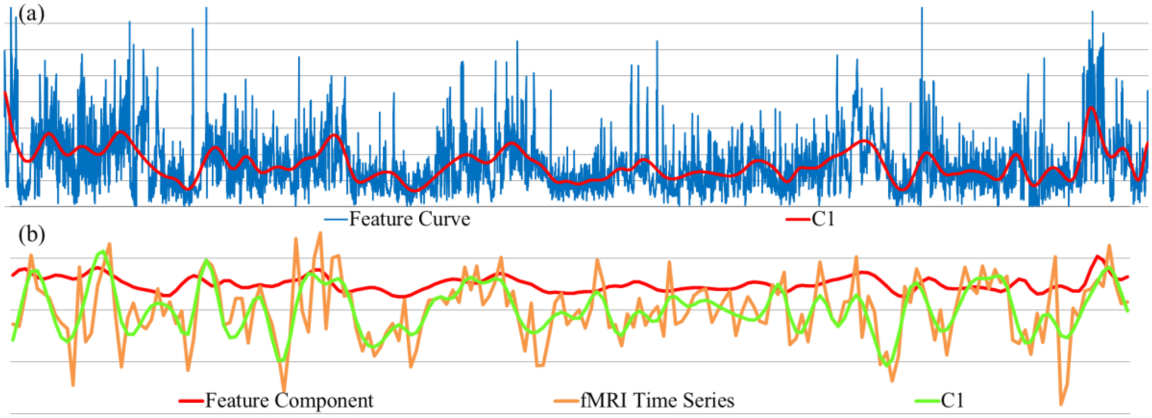

Fig. 2.14. Low-level features in natural stimulus fMRI. (a) Decomposition of the visual motion saliency feature curve into a coarser-scale signal (C1); (b) Comparison of the extracted visual low-level feature component and the fMRI component at similar scales.

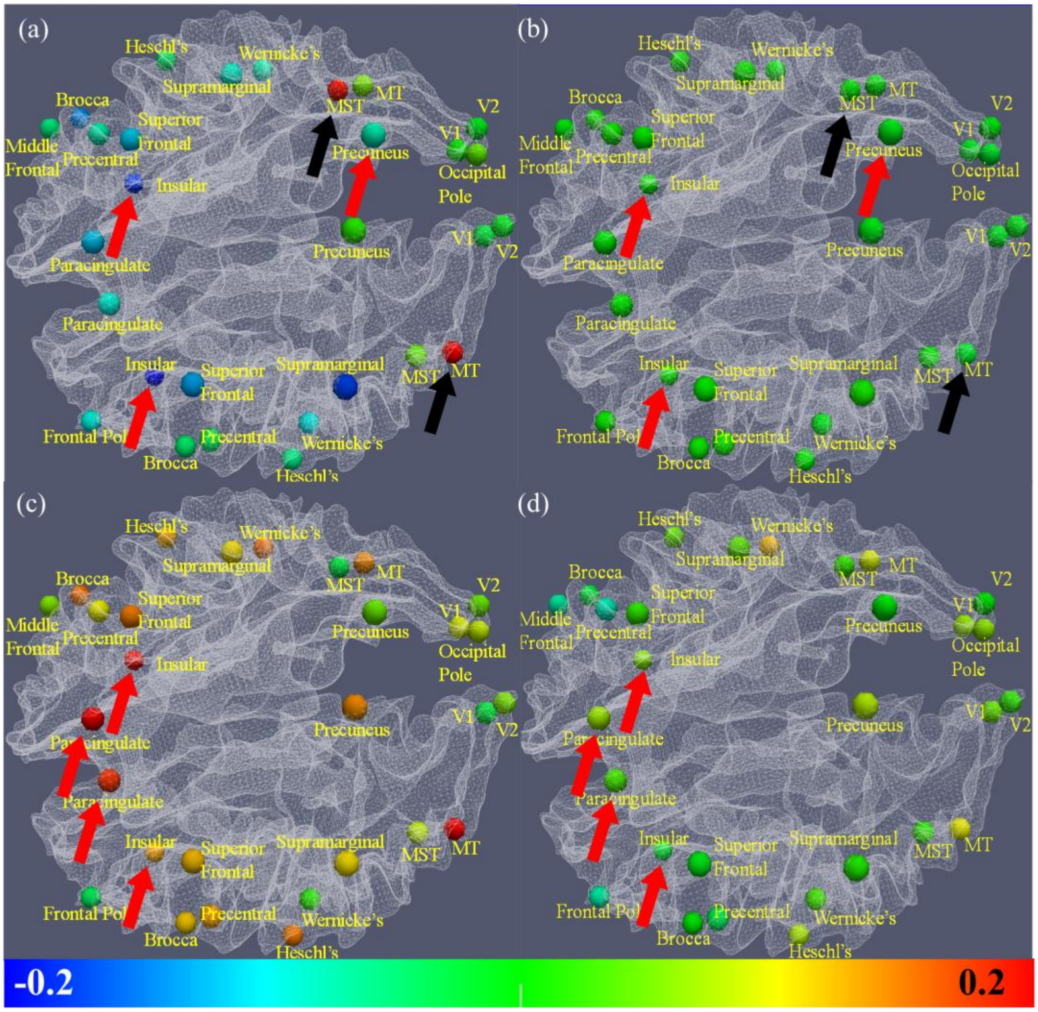

Fig. 2.15. EMCD on natural stimulus fMRI. EMCD-derived correlation (a) and Pearson correlation (b) between visual motion saliency feature curve and fMRI time series. EMCD-derived correlation (c) and Pearson correlation (d) between logarithm audio signal energy feature curve and fMRI time series. The color bar is at the bottom. The arrows in the same colors highlighted some brain regions with significant differences between the two methods in (a) and (b), as well as in (c) and (d). The correlation is much stronger between the visual motion saliency feature and brain regions for motion perception, including MT and MST (black arrows), while negative correlation was exposed for insular and precuneus (red arrows and blue bubbles in (a)). When comparing with logarithm audio signal energy feature, insular and paracingulate exhibited strong correlation (c). The corresponding Pearson correlation results shown in (b) and (d) could not reveal the differences.

EMCD in Natural Stimulus fMRI Analysis

Natural stimulus fMRI of movie watching allows us to continuously monitor the brain's responses to multimedia contents in a natural way and with high spatial resolution. Importantly, recent research studies [54, 62, 63], have shown that natural stimuli provide a realistic experiment environment for brain research and that the human brain's response to the same stimulus is reliable and reproducible across individuals. In the literature, a relatively less explored issue in natural stimulus fMRI is how to measure the correlation between low-level feature curves extracted from continuous audio/video streams, such as motion energy and motion saliency [58], and fMRI BOLD signals. In our experiments, we applied the EMCD framework to measure the correlation between multi-scale low-level multimedia feature curves and fMRI signals, in order to elucidate the potential correlative interactions among multimedia stimuli and the human brain's perception and cognition [54, 62, 63].

The frequencies of fMRI signals and low-level multimedia features are at quite different scales, e.g., 0.1Hz vs. 30Hz. Hence, we extracted the components from fMRI time series, and use the scale information to guide the decomposition of low-level multimedia feature curves to obtain components at the similar scale. Depicted in Fig. 2.14a is an example of decomposing the visual motion saliency features [58] into a coarser-scale signal. After the decomposition, the extrema time points were kept and the extracted component was later reconstructed at the length of the fMRI time series with the extrema for the correlation analysis.

Then, the correlation between these two types of signals are measured by the Pearson correlation of corresponding EMCD components at the same or similar temporal scales, as illustrated in Fig. 2.14b. We hypothesize that low-level features with specific semantic meanings will have higher correlations with the corresponding signals from relevant brain regions. For instance, Fig. 2.15a shows a pilot result on visual motion saliency features, from which we can see that much stronger correlation appears in some brain regions for motion perception including right middle temporal (MT) region and left middle superior temporal (MST) region [64] (black arrows in Fig. 2.15a), when we compared the EMCD C_1 components of fMRI BOLD signals and the visual saliency feature curve [58]. The result is quite reasonable, given current known neuroscience knowledge that MT and MST regions are responsible for visual motion processing and understanding [64]. As a comparison, we calculated the Pearson correlation between the original visual saliency feature and the raw fMRI time series signals and it turns out that most correlations are close to zero, indicating that calculating the Pearson correlation between original fMRI signals and low-level multimedia features at different time scales is unable to infer any meaningful information (Fig. 2.15b).

In addition to the capability of inferring meaningful positive correlations between fMRI signals of MT and MST brain regions and the visual motion saliency features, interestingly, our EMCD-based method also reveals strong negative correlation between the visual saliency feature and the fMRI signal of the insular and precuneus regions (red arrows in Fig. 2.15a), while the measured Pearson correlation between the original raw fMRI signals and visual motion saliency features cannot. The validity of the results on negative correlations for insular and precuneus regions in Fig. 2.15a is supported by a variety of literature neuroscience studies that reported the deactivation of vestibular cortex (including insular and precuneus regions) in response to visual motion [65-67].

In addition to visual low-level features, Fig. 2.15c shows another result of the correlation between logarithm audio signal energy feature curve and fMRI time series, where the insular and paracingulate regions (red arrows in Fig. 2.15c) exhibit strong positive correlation with the audio features. The validity of these results is supported by several neuroscience literature studies that reported activations of these regions in response to audio stimuli [68-72]. However, the results by calculating the Pearson correlation between the raw low-level auditory feature curves and fMRI signals are close to zero (Fig. 2.15d).

The promising results in Fig. 2.15 indicate that the EMCD-based correlation analysis is able to discover meaningful intrinsic positive/negative correlations between low-level multimedia features and fMRI signals extracted from relevant functional brain regions. The critical point here is that the EMCD enables the decomposition of time series into components of multiple temporal scales so that the correlative structure can be measured at the same or similar scales.

CHAPTER 3

FUNCTIONAL ROLES OF CORTICAL GYRI AND SULCI

3.1 Functional Mechanisms of the Human Brain

We qualitatively and quantitatively analyzed two independent multimodal DTI/R-fMRI (resting state fMRI) datasets to test our proposed functional model of the human brain, that is, *gyri are the global functional integration hubs and sulci are the local functional units*. Specifically, the pre-central gyrus (PCG), post-central gyrus (POG), central sulcus (CS), and post-central sulcus (PCS) on both of the left and right hemispheres were labeled. Their structural and functional connectivity were examined based on multimodal DTI/R-fMRI data. Our rationale is that the PCG, POG, CS and PCS are within the primary motor and primary somatosensory systems and are known to possess structural and functional connections [5]. Thus, this well-characterized sub-system of the cerebral cortex can serve as a test-bed to investigate the functional mechanisms of cortical gyri and sulci. Furthermore, the whole-brain functional connectivity to the landmarks on these selected gyri/sulci are also measured and examined. The extensive experimental results from two independent multimodal DTI/R-fMRI datasets have consistently demonstrated the following findings. First, there exists strong functional connectivity between any pair of the four gyri. Second, the functional connectivity among four sulci is relatively weak except between LCS (L- for left) and RCS (R- for right). Third, the functional connectivity between neighboring gyri and sulci are moderate. These three lines of experimental findings have been replicated by two independent multimodal DTI/R-fMRI datasets and were further confirmed by whole-brain analyses, thus supporting our hypothesized functional model of cortical gyri and sulci: gyri serve as the global functional integration hubs, while sulci function as the local functional units.

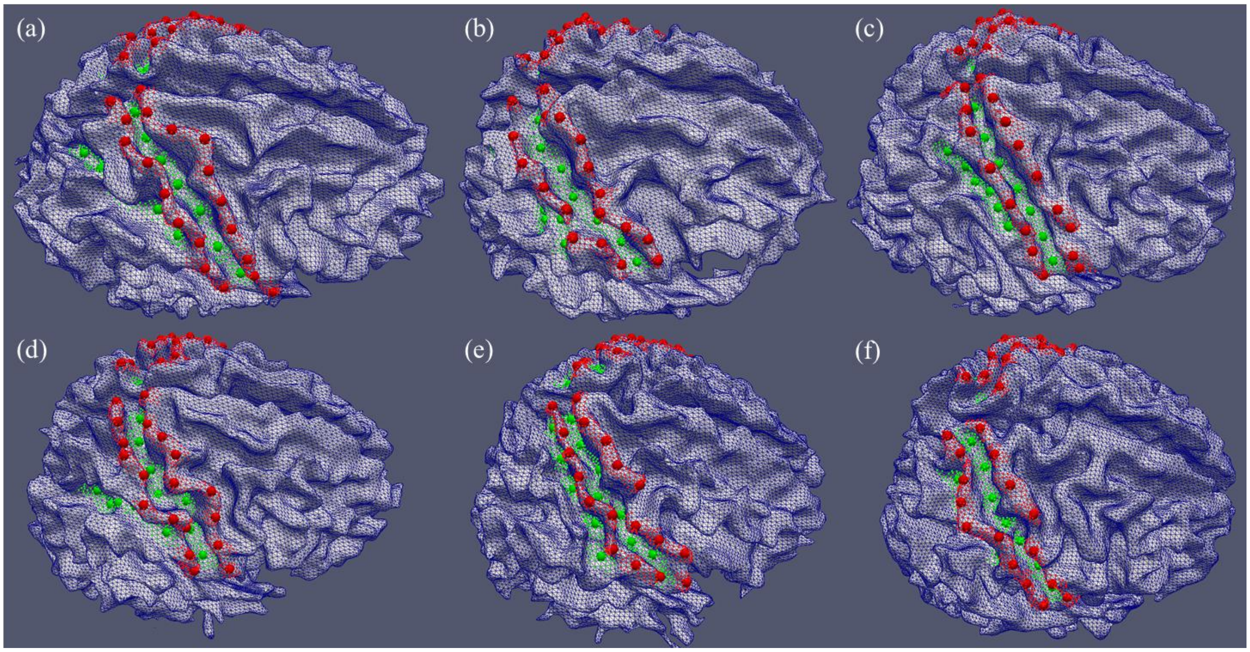

Fig. 3.1. Placements of landmarks on cortical gyri and sulci. Initial landmarks (color bubbles) were chosen manually on the cortical surface for a roughly uniform distribution on the gyrus or sulcus. Other algorithm-generated sample landmarks are shown in small red/green dots. Six examples are shown in this figure.

3.2 Joint Multimodal Representation

Labeling landmarks on cortical gyri and sulci

Cortical segmentation of gyri and sulci based on structural MRI images has been extensively studied in the neuroimage analysis literature [7, 10-15], and a variety of algorithms and software tools are available. In this thesis, however, we used the cortical surfaces reconstructed from DTI images to reduce the misalignment between fMRI images and structural images due to the geometric distortions that are commonly expected in EPI sequences [26, 50, 73, 74]. The reconstructed surfaces, however, are of lower quality because of the lower resolution of DTI data (2 mm isotropic) in comparison with structural T1-weighted MRI images (1 mm isotropic). The automatic methods might not be able to robustly extract gyral/sulcal patches. To ensure good quality of landmark labeling, visual inspection was used to interactively determine the four gyral and sulcal surface patches. Then, a series of structural landmarks (the number ranges from five to ten as shown in Table 3.1) were placed on those identified gyri and sulci, as shown in Fig. 3.1.

Table 3.1. NUMBER OF LABELED LANDMARKS PER CORTICAL REGION.

		LPCG	LPOG	LCS	LPOS	RPCG	RPOG	RCS	RPOS
Dataset 1	Mean	9.18	8.55	7.55	5.91	9.09	8.82	7.36	5.64
	Stdev	0.98	1.13	0.93	0.94	2.59	1.54	0.81	0.92
Dataset 2	Mean	10.00	9.25	8.38	7.13	9.75	9.13	8.00	7.25
	Stdev	1.07	1.28	0.92	1.25	1.91	1.46	0.53	1.16

It should be noted that at current stage, there are no structural and/or functional correspondences between the landmarks in different subjects due to the lack of mature algorithms or tools (as far as we know) that can reliably achieve those correspondences. Thus, the structural and functional correspondences across different brains have to be established at the gyrus/sulcus level, instead of the landmark level, and thus the proposed functional model is at the level of cortical gyri and sulci as well. Due to this lack of correspondences of cortical landmarks across different brains, examining the functional connectivity of cortical gyri/sulci based solely on the manually extracted cortical landmarks could potentially be biased. That is, the manually placed landmarks and their representative fMRI time series might not be sufficient to represent the functional activities of a whole gyrus or sulcus. In addition, due to the variability, nonlinearity, and inhomogeneity of the cerebral cortex, a slightly displaced landmark, even by only a few surface vertices, could have quite different structural and/or functional connectivity profiles, as demonstrated in [20, 23, 50]. Therefore, in order to reduce the potential bias and ensure sufficient statistical power, we algorithmically generated additional 100 different sets of sample landmarks for each subject based on the manually-labeled landmarks. Specifically, this procedure serves as a repeated uniform sampler on the three-ring surface mesh neighborhoods in terms of graph connectivity of the original manually-labeled landmarks. In each repetition, the procedure randomly picks one vertex within the three-ring surface mesh neighborhood of each landmark with equal probability. The newly selected vertices form a new set of landmarks with the same number of elements as the original manually-labeled landmarks, as represented by the red and green dots in Fig. 3.1. It can be seen from the figure that the sampled landmarks constitute a dense coverage of the whole gyrus/sulcus. Even if some of the manually-labeled landmarks were misplaced, the above sampling procedure can substantially reduce the potential bias by including many more additional neighboring sampled landmarks and ensure the statistical power. These sampled landmarks were then used to localize the R-fMRI time series under structural guidance, as detailed in [50]. To increase signal-to-noise ratio, each sampled landmark is represented by the average of R-fMRI time series within a one-ring surface mesh neighborhood. The numbers of labeled landmarks in the gyri/sulci in two independent datasets are provided in Table 3.1.

Joint multimodal representation methodology

Our previous studies [26, 27] have shown that axonal fiber connections closely follow the gyral folding patterns. This observation has been replicated in all of the DTI datasets of human, chimpanzee, and macaque brains we analyzed [26, 27]. Therefore, for each gyral or sulcal landmark defined in Fig. 3.1, the emanating fibers connected to the landmark in consideration can be readily extracted from the results of whole-brain streamline tractography via a similar method detailed elsewhere [20, 23, 52]. In addition, the R-fMRI signals can also be extracted for each vertex within the neighborhood of the landmark in consideration, and then averaged to represent the functional activity of that landmark [50]. As a result, the structural fiber connections and R-fMRI signals for each gyral and sulcal landmark are co-localized on and jointly represented by the same cortical surface patch. This joint representation of cortical shape, structural connection, and functional activity effectively takes the advantage of the fact that multimodal DTI and R-fMRI data are in the same DTI space and exhibit much less geometric misalignment [20, 50]. That is, the geometric distortions in EPI (echo planar imaging)-based DTI and R-fMRI tend to be similar [50], which substantially reduces the misalignment between traditionally used structural MRI and DTI/fMRI images [26, 74]. Additionally, this joint multimodal representation methodology enables and facilitates simultaneous modeling of structural and functional connectivity of cortical landmarks, thus offering important insights into the structural and functional brain architectures and their functional mechanisms.

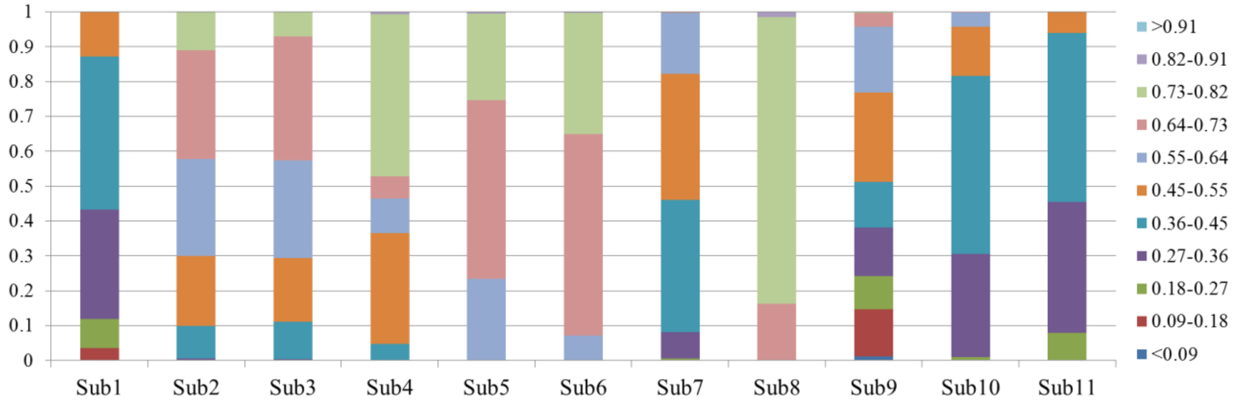

Fig. 3.2. Distributions of FC values (without normalization) for each subject in dataset 1. The distributions, though are Gaussian-like, differ substantially.

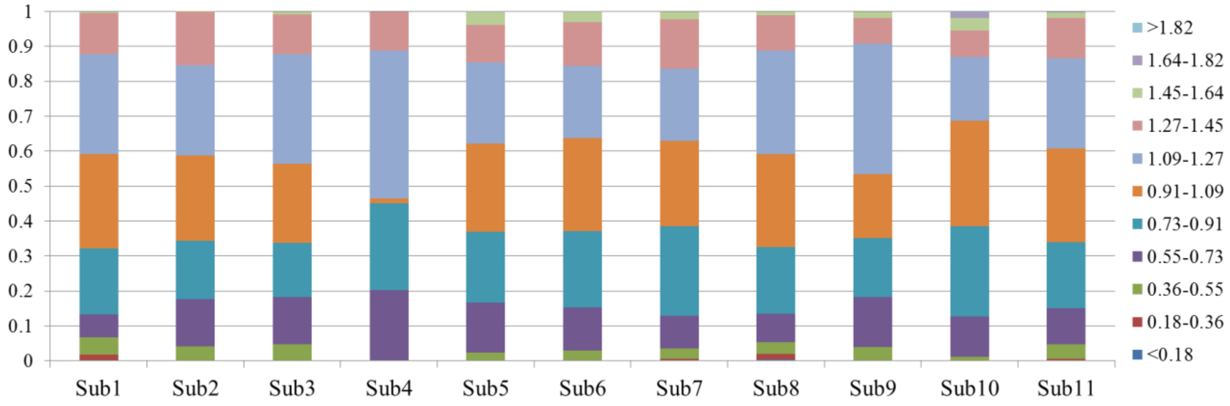

Fig. 3.3. Distributions of normalized FC values for each subject in dataset 1. In comparison with the raw correlation distributions in Fig. 3.2, the normalization procedure results in consistent individual distributions and enables fair comparisons of results from different subjects.

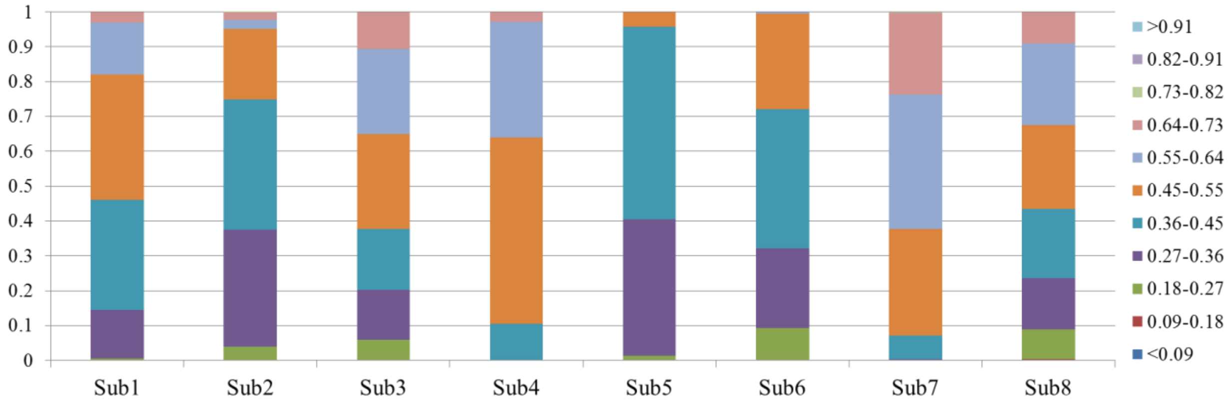

Fig. 3.4. Distributions of FC values (without normalization) for each subject in dataset 2. The distributions, though are Gaussian-like, differ substantially.

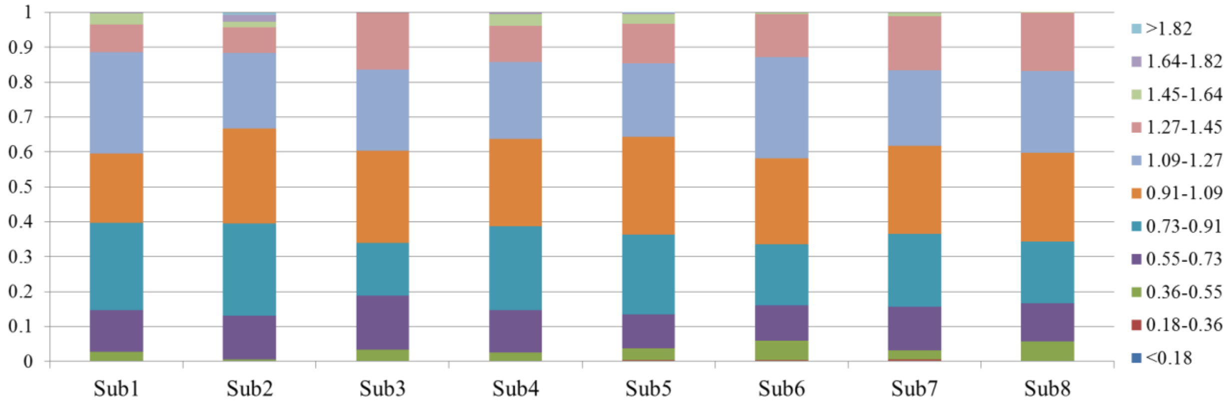

Fig. 3.5. Distributions of normalized FC values for each subject in dataset 2. In comparison with the raw correlation distributions in Fig. 3.4, the normalization procedure results in consistent individual distributions and enables fair comparisons of results from different subjects.

Structural/functional connectivity among gyral/sulcal landmarks

For a pair of the gyral/sulcal regions, their functional correlation strength was calculated by averaging the functional connectivity between any possible pairs of landmarks on two cortical regions. Here, the Pearson correlation [50] between two extracted R-fMRI signals from two cortical landmarks was considered as their functional connectivity. In order to gain robustness and full coverage of the whole gyrus/sulcus, 100 sets of sampled landmarks were randomly selected in the 3-ring surface mesh neighborhood of the corresponding landmark (e.g. Fig. 3.1).

This procedure creates 100 functional connectivity matrices for each subject and they were averaged element-wise to suppress noise and outliers, resulting in a final functional connectivity matrix for each subject. It should be noted that the distributions of functional correlation values could vary largely from subject to subject, as demonstrated in Fig. 3.2 and Fig. 3.4 (for two different datasets). Therefore, we used the mean functional correlation value and the standard deviation per subject to normalize the corresponding subject's functional connectivity correlation matrix. As a result, this normalization procedure provides much more consistent and comparable individual distributions, as shown in Fig. 3.3 and Fig. 3.5 (for the same two datasets), and enables fair comparisons of functional connectivity between different subjects. The normalized functional connectivity matrices are then used in subsequent analyses. Intuitively, a value of 1.0 represents an average functional connection level, and the larger the value is, the stronger the functional connectivity will be.

To extract the DTI-derived white matter fibers connecting to a certain gyral/sulcal landmark, the fibers in the 3-ring surface mesh neighborhood of each landmark were collected via a similar approach in [20, 23]. Then, the structural connectivity strength between two cortical regions is represented by the number of fibers connecting both regions [19, 20, 75]. Similar to the normalization procedure in measuring functional connectivity, the structural connection strength was normalized by the average number of fibers between any pair of cortical landmarks in this study, in order to reduce the individual variability. Thus, a value of 1.0 represents the average structural connectivity; the larger the value is, the stronger the structural connectivity will be. Finally, the structural or functional connection strength between any pair of cortical gyri/sulci is defined as the averaged connection strength between all possible combinational pairs of the landmarks on two gyri/sulci. Details of the abovementioned algorithms are covered in section 3.3.

3.3 Methods

Labeling landmarks on gyri and sulci

The cortical landmarks were manually labeled and placed as shown in Fig. 3.1. Specifically, each subject's reconstructed cortical surface mesh was visualized in ParaView [76] using the built-in "Surface With Edges" display mode. The gyri and sulci to be extracted were visually identified by experts. A number of landmarks were chosen at surface mesh vertices that are distributed roughly evenly along the ridges of gyri and the valleys of sulci (color bubbles in Fig. 3.1). The number of landmarks for a specific gyrus/sulcus is dependent on the size of the cortical region (Table 3.1).

Assessing functional connectivity

For each pair of cortical gyrus/sulcus, their functional correlation was obtained by averaging the absolute value of Pearson correlations of the R-fMRI time series of any possible pair of landmarks drawn from both regions. Specifically, given two gyral/sulcal regions X and Y, the landmarks $x_1 \ldots x_m$ on X, and the landmarks $y_1 \ldots y_n$ on Y, their functional correlation (FC) between X and Y is calculated as:

Equation 3.1

$$FC(X,Y) = \frac{1}{mn} \sum_{i=1}^{m} \sum_{j=1}^{n} \left| Pcorr(x_i, y_j) \right|$$

where Pcorr denotes the Pearson correlation of the R-fMRI time series of two landmarks. This FC value represents the average of functional correlation between two gyral/sulcal regions with the selected landmarks.

For each set of sample landmarks, we obtain a symmetric eight-by-eight FC matrix and thus 100 matrices per subject by including the algorithm-sampled landmarks. Then, the functional connectivity was averaged in terms of pair-wise FC value to reflect the overall correlation level of two cortical regions at the gyri/sulci level.

Table 3.2. AVERAGE FC VALUES IN INDIVIDUAL SUBJECTS.

	Sub	1	2	3	4	5	6	7	8	9	10	11	Stat
Dataset 1	Mean	**0.37**	0.60	0.60	0.64	0.69	0.71	0.47	**0.76**	0.41	0.40	0.37	**0.55**
	Stdev	0.08	0.10	0.10	0.13	0.06	0.05	0.08	0.03	0.17	0.07	0.06	**0.15**
Dataset 2	Mean	0.46	0.40	0.48	0.52	**0.38**	0.40	**0.57**	0.47				**0.46**
	Stdev	0.09	0.09	0.13	0.06	0.05	0.08	0.08	0.13				**0.07**

Table 3.2 shows the average FC values of individual subjects used in our analysis. From the table we can see that: (1) in dataset 1 the average FC varies from the lowest 0.37 (subject 1) to the highest 0.76 (subject 8, twice as that in subject 1); while in dataset 2 the range is from 0.38 (subject 5) to 0.57 (subject 7); (2) the standard deviations are 0.15 and 0.07 for dataset 1 and 2, respectively, which is considered substantial given that the mean values are 0.55 and 0.46. To overcome this remarkable variability across subjects, we normalize the functional connectivity by the average FC values and standard deviation of individuals. For each subject, the functional connectivity values, FC, in the averaged functional network is normalized by

Equation 3.2
$$\overline{FC(X,Y)} = 1 + \frac{FC(X,Y) - \mu}{4\sigma}$$

where μ is the average FC of the corresponding subject; σ is the standard deviation; 4σ, as commonly used in statistics, is considered as a cut-off threshold of the Gaussian distribution (experimental results suggested that the histograms of the FC are similar to Gaussian distributions). With this normalization scheme, a functional connection with strength equivalent to the average level of the subject will have a value of 1.0. As a comparison, the distributions of FC values and those of the normalized values for each subject are shown in Fig. 3.2 and Fig. 3.3, respectively, for dataset 1, and Fig. 3.4 and Fig. 3.5, respectively, for dataset 2. These figures further confirmed that before normalization (Fig. 3.2 and Fig. 3.4), the distributions of FC values vary largely across individuals. It is infeasible to directly compare the results obtained from different subjects. Instead, the normalization procedure described above brings consistency to the distributions (Fig. 3.3 and Fig. 3.5). The distributions after normalization are similar to each other and thus enable fair comparisons across subjects. In the following sections, the normalized values will be used in our analysis. These normalized matrices are further averaged together to form a single eight-by-eight functional connectivity matrix, which is used in our modeling and analyses of functional roles of gyri and sulci.

Graph analysis

The functional network of cortical gyri and sulci is considered as a graph, and the functional connectivity is regarded as a weight for each edge in the graph. For each functional network that is generated by a set of sample landmarks, we examined the edge degrees defined as the number of edges with a weight (functional connectivity) larger than 1. These edge degrees were accumulated for each cortical gyral/sulcal region that the node belongs to in the repeated experiments. The accumulated edge degrees were then normalized based on an individualized profile, where zero means no connection at all and one means the node has connection edges to every other node.

Whole brain connectivity analysis

In the whole brain connectivity analysis, only the original manually labeled landmarks (e.g. the bubbles in Fig. 3.1) were used. For each landmark, the averaged R-fMRI time series within its 3-ring surface mesh neighborhood is chosen to represent the landmark for the purpose of increasing the signal-to-noise ratio. Then, the functional connectivity between the landmark in consideration and any other cortical voxel on the whole cerebral cortex is measured using either

Wavelet transform or Pearson correlation (details in subsequent sections) between the two R-fMRI time series, thus generating a whole-brain functional connectivity map for each landmark.

We applied the above approaches to generate the cortical connectivity maps for all of the manually labeled landmarks, and selected the top 1% of the most functionally correlated cortical voxels for each landmark. The 1% threshold is selected so that: 1) we have sufficient cortical voxels to ensure statistical power (approximately 500 cortical voxels per subject for dataset 1 and 900 voxels per subject for dataset 2); and 2) the selected cortical voxels are likely to be truly functionally connected. Then, these selected cortical voxels were classified into gyral and sulcal ones [77], and the ratios of the numbers of strongly correlated gyral voxels over those of strongly correlated sulcal voxels were reported.

3.4 Experiment Data

Dataset 1

Eleven healthy volunteers were scanned in a GE 3T Signa MRI system (GE Healthcare, Milwaukee, WI) using an 8-channel head coil at the Bio-imaging Research Center (BIRC) of the University of Georgia (UGA) under IRB approval. The experiments were undertaken with the understanding and written consent of each subject. DTI data was acquired using the spatial resolution 2 mm × 2 mm × 2 mm; parameters are TR 15.5s and TE min-full, b-value=1000 with 30 DWI gradient directions, and 3 B0 volumes were acquired. R-fMRI data was acquired using dimensionality 128×128×60×100, spatial resolution 2 mm × 2 mm × 2 mm, TR 5s, TE 25 ms, and flip angle 90 degrees [50]. All DTI and R-fMRI scans were aligned to the AC-PC line. For the anatomic MRI data, pre-processing includes brain skull removal, and gray matter (GM) and white matter (WM) tissue segmentation [74]. Then the GM/WM cortical surfaces were reconstructed using the marching cubes algorithm [78]. For the DTI data, pre-processing includes brain skull removal, motion correction, and eddy current correction [20]. Fiber tracts were generated from the DTI data by using MedINRIA [79]. Pre-processing of the R-fMRI data includes brain skull removal, motion correction, spatial smoothing, temporal pre-whitening, slice time correction, global drift removal, and band pass filtering (0.01 Hz to 0.1 Hz) [50].

Dataset 2

The second multimodal DTI/R-fMRI dataset includes eight healthy brains from the publicly available NA-MIC dataset [80]. The multimodal DTI/R-fMRI imaging parameters are as follows. Both DTI and R-fMRI scans were acquired on a 3 Tesla GE system using echo planar imaging sequences. An eight-channel coil was used to perform parallel imaging using ASSET (Array Spatial Sensitivity Encoding Techniques, GE) with a SENSE-factor (speed-up) of 2. The DTI parameters are: 51 directions with b=900, 8 baseline scans with b=0, TR 17000 ms, TE 78 ms, FOV 24 cm, 144×144 encoding steps, and 1.7 mm slice thickness. Totally, 85 axial slices parallel to the AC-PC line covering the whole brain were acquired. The R-fMRI scan is 10 minutes long, and contains 200 repetitions of a high resolution EPI scan. The parameters are: 96 × 96 in plane, 3 mm thickness, TR=3000 ms, TE=30, 39 slices, and ASSET. During R-fMRI scans, the subjects kept their eyes closed and rested. Pre-processing of this DTI/R-fMRI dataset is similar to that of the first dataset [20]. This second dataset is used as an independent dataset to replicate the findings from the first dataset.

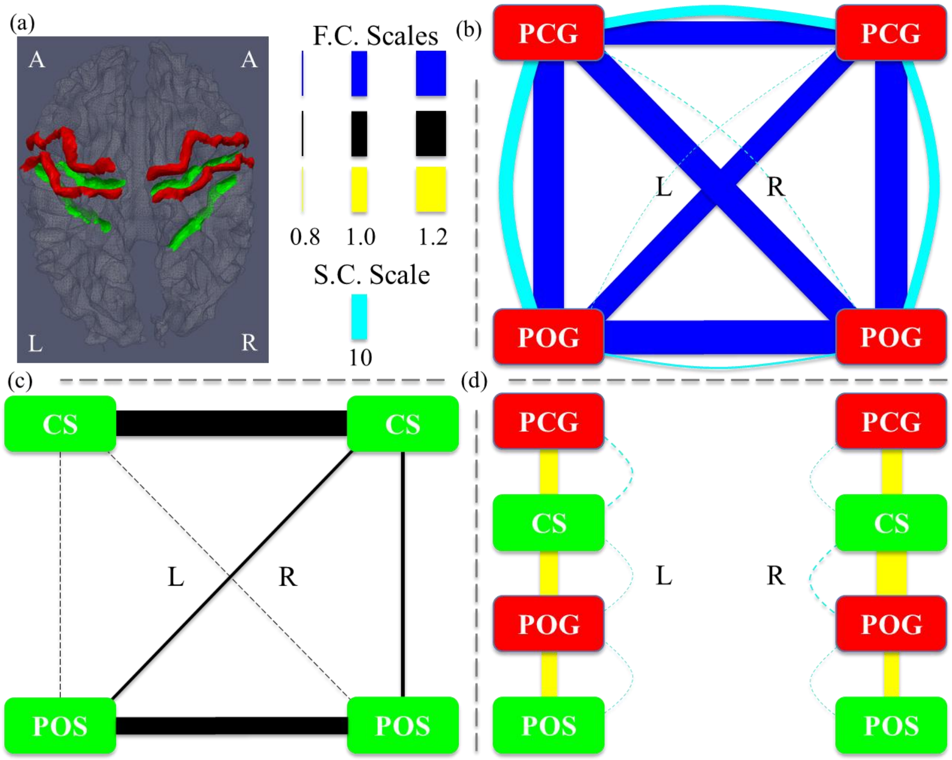

Fig. 3.6. Structural/functional connectivity among pre- and post-central gyri/sulci. (a) Illustration of the four gyral regions (red) and four sulcal regions (green). In (b)-(d), the width of a functional connection edge, blue for gyri-gyri pattern in (b), black for sulci-sulci pattern in (c), and yellow for gyri-sulci pattern in (d), is proportional to the functional connectivity (F.C.). The width of a structural connection edge (cyan) is proportional to the structural connectivity (S.C.). The right panel shows: (1) the size of functional edges with 80% of, 100% of, and 120% of average functional connectivity, respectively; and (2) the structural edges with ten times of the average number of fibers connecting a pair of cortical landmarks (a structural connectivity value of 10.0). Weak edges (width less than one) are in dashed lines. (b) Joint representation of structural and functional connectivity among four gyri. Strong structural connectivity was observed in LPCG-LPOG, RPCG-RPOG, and LPCG-RPCG. (c) Joint representation of structural and functional connectivity among four sulci. No or very weak structural connectivity was observed from the DTI data. (d) Joint representation of structural and functional connectivity between adjacent gyri and sulci.

Table 3.3. Gyral Structural/Functional Connectivity in Dataset 1[i].

Con Sub	Functional Connectivity						Structural Connectivity					
	LPCG RPCG	LPCG RPOG	LPCG LPOG	RPCG LPOG	RPCG RPOG	LPOG RPOG	LPCG RPCG	LPCG RPOG	LPCG LPOG	RPCG LPOG	RPCG RPOG	LPOG RPOG
1	1.25	1.30	1.34	1.19	1.26	1.27	7.08	0.00	4.61	0.00	12.02	0.00
2	1.30	1.30	1.26	1.27	1.36	1.33	4.64	0.93	5.93	0.56	12.98	0.93
3	1.06	1.20	1.38	1.12	1.11	1.37	8.48	3.15	8.85	0.00	5.94	0.85
4	1.26	1.25	1.27	1.23	1.29	1.29	6.05	0.00	11.35	0.76	6.81	0.38
5	0.61	0.86	1.00	0.93	1.14	1.28	4.81	0.00	8.75	0.00	6.56	0.44
6	1.22	1.13	1.39	1.40	1.19	1.30	12.73	0.00	3.39	0.85	1.70	2.55
7	0.91	1.22	1.41	0.98	1.00	1.33	2.49	0.00	18.36	0.00	5.29	0.62
8	1.11	1.17	0.97	0.80	1.07	1.04	2.77	0.35	11.06	0.00	4.49	5.88
9	1.15	1.19	1.24	1.09	1.21	1.25	7.00	0.78	9.72	0.00	8.17	0.39
10	1.09	1.12	1.10	1.13	1.64	1.15	9.12	1.00	5.69	0.84	6.49	2.37
11	1.22	1.17	0.99	0.77	1.33	1.20	7.11	1.64	10.49	0.18	4.74	0.09
Mean	1.11	**1.17**	**1.22**	1.08	**1.24**	**1.26**	**6.57**	0.71	**8.93**	0.29	**6.84**	1.32
Stdev	0.20	0.12	0.17	0.20	0.17	0.09	2.95	0.98	4.14	0.38	3.26	1.73
p-val	0.10	**0.00**	**0.00**	0.19	**0.00**	**0.00**	**0.00**	0.82	**0.00**	1.00	**0.00**	0.28

3.5 Results

Structural/functional connectivity among four gyri

The structural and functional connection patterns among four gyri (red ribbons in Fig. 3.6a) are shown in Fig. 3.6b. A major observation from the gyrus-gyrus connection patterns in Fig. 3.6b is that there exist both strong structural (cyan curves) and functional (blue lines) connectivity among those selected gyri. For instance, the DTI-derived structural fiber connections between PCG and POG on both hemispheres are quite strong, and their functional connections are strong as well. From a neuroanatomy perspective, this result is quite reasonable since the primary motor cortex (PCG) and primary somatosensory cortex (POG) are known to have strong connections [5]. This DTI study also demonstrates that there is strong direct structural connection between PCGs on two hemispheres, while the direct structural connections between LPOG and RPOG is relatively weak, as shown in Fig. 3.6b. However, it is interesting

---

[i] Statistically significant elements are underlined (p-value<0.05, one-sample, two-tailed test, mean=1.0 for functional connectivity; one-sample, right-tailed test, mean=1.0 for structural connectivity). The same parameters apply to subsequent tables of connectivity.

that the functional connection between LPOG and RPOG is still strong. Our interpretation is that this strong functional connection might attribute to the strong *indirect* structural connections through LPCG and RPCG. This result provides supporting evidence to the notion of functional connectivity via *indirect* structural connections that have been examined in the literature [81]. Our interpretation that strong *indirect* structural connection underlies strong functional connection is further supported by the strong functional connections between LPCG and RPOG and those between RPCG and LPCG, though the direct structural connections between them are relatively weak, as shown by the dashed cyan curves in Fig. 3.6b.

Quantitative measurements of these structural and functional connection strengths between any pair of gyri in the eleven subjects in dataset 1 are shown in Table 3.3. It is apparent that the functional connection strength of any pair of gyri is above 1, meaning that the functional connection strengths between gyral regions are all above average. In particular, four pairs exhibit statistical significance ($p\text{-value}<0.05$) and they are underlined in the left panel of Table 3.3. This result quantitatively demonstrates that gyral regions interact strongly with other gyral regions (at least the ones we studied here), supporting our hypothesized functional model of cortical gyri. From the right panel in Table 3.3, it can also be found that there are strong or weak direct structural connections among any pair of gyri. In particular, there are three pairs of strong direct structural connections (LPCG-RPCG, LPCG-LPOG, and RPCG-RPOG), as highlighted by the underlines in the right panel of Table 3.3. In comparison, other pairs of gyri (LPCG-RPOG, RPCG-LPOG, and LPOG-RPOG) exhibit relatively weak direct structural connections. The functional connection strengths for these pairs, however, are still strong, as shown in the left panel of Table 3.3, and their indirect structural connections are strong as well (defined as successive strong direct connections, up to 3-hops here). This result further suggests that: 1) strong indirect structural connections are associated with strong functional connectivity [18, 81]; and 2) structural and functional connectivity are closely related [6, 18, 20, 82]. Notably, an important differentiation that should be made here is the particularly evident close relationship between strong functional connectivity and strong direct/indirect structural connections for gyrus-gyrus pairs.

Table 3.4. SULCAL STRUCTURAL/FUNCTIONAL CONNECTIVITY IN DATASET 1.

Con / Sub	Functional Connectivity						Structural Connectivity					
	LCS RCS	LCS RPOS	LCS LPOS	RCS LPOS	RCS RPOS	LPOS RPOS	LCS RCS	LCS RPOS	LCS LPOS	RCS LPOS	RCS RPOS	LPOS RPOS
1	1.14	0.45	0.82	0.68	0.40	0.81	0.00	0.00	0.00	0.00	0.00	0.00
2	1.11	0.50	0.61	0.72	0.61	0.84	0.00	0.00	0.00	0.00	0.00	0.00
3	1.18	0.57	0.94	0.88	0.56	0.76	0.00	0.00	0.00	0.00	0.00	0.00
4	1.15	0.71	0.65	0.62	0.74	0.79	0.00	0.00	0.00	0.00	0.00	0.00
5	1.27	0.93	0.71	0.89	1.26	1.21	0.00	0.00	0.00	0.00	0.00	0.00
6	1.02	0.64	0.82	0.83	0.69	1.25	0.00	0.00	0.00	0.00	0.00	0.00
7	0.87	0.80	0.78	0.92	1.01	1.31	0.00	0.00	0.00	0.00	0.00	0.00
8	1.33	0.94	1.16	1.18	1.17	1.27	0.00	0.00	0.00	0.00	0.00	0.00
9	1.45	0.57	0.54	0.57	0.62	1.05	0.00	0.00	0.00	0.00	0.00	0.00
10	0.74	0.78	0.72	0.99	1.17	0.90	0.00	0.00	0.00	0.00	0.00	0.00
11	1.24	0.51	0.61	0.80	0.87	1.03	0.00	0.00	0.09	0.00	0.00	0.00
Mean	1.14	**0.67**	**0.76**	**0.82**	0.83	1.02	**0.00**	**0.00**	**0.01**	**0.00**	**0.00**	**0.00**
Stdev	0.20	0.17	0.17	0.18	0.29	0.21	0.00	0.00	0.03	0.00	0.00	0.00
p-val	0.05	**0.00**	**0.00**	**0.01**	0.07	0.77	1.00	1.00	1.00	1.00	1.00	1.00

Structural/functional connectivity among four sulci

The structural and functional connection patterns among four selected sulci are shown in Fig. 3.6c. It is evident that there is no or extremely weak DTI-revealed direct structural connection between any pair of sulcal regions (no cyan curves in Fig. 3.6c). This result further replicates our prior results reported in [26, 27] that axonal fiber connection terminations concentrate on gyri, but not on sulci. Meanwhile, the functional connections of the sulci pairs of LCS-RPOS, LCS-LPOS, RCS-LPOS, and RCS-RPOS are week (black lines in Fig. 3.6c), suggesting that weak functional connections are associated with no direct structural connections and weak indirect structural connections. This result supports our hypothesized functional model: sulci are the local functional units. It is interesting that the RCS-LCS pair has relatively higher functional connection. Our interpretation is that both RCS and LCS are connected to the RPCG and LPCG through local inter-column cortico-cortical axons, and RPCG and LPCG are strongly connected by structural axonal fibers (Fig. 3.6b). As a result, RCS-LCS has relatively strong indirect structural connections, and therefore exhibits stronger functional connectivity. These results further suggest that functional connectivity has its structural underpinnings. For instance, weak direct structural connections predict weak functional connectivity, as shown by the sulcus-sulcus connection patterns in Fig. 3.6c and Table 3.4. If there is a strong indirect structural connection, however, the functional connectivity could be strong, as demonstrated by the RCS-LCS connection patterns.

The quantitative measurements of these structural/functional connection strengths are provided in Table 3.4. It is evident that in all of the eleven subjects we studied, there is no or very weak structural connections between any pair of sulci, which is consistent with our previous reports in [26]. Also, the functional connection strengths between LCS-RPOS, LCS-LPOS, RCS-LPOS, and RCS-RPOS are substantially lower than the average, and three of them are statistically significant, as underlined in the left panel of Table 3.4. The LCS-RCS pair has higher functional connection, which was already interpreted and explained in the previous paragraph. Therefore, the results in this section have demonstrated that sulcal regions have much less remote functional interactions with other sulcal regions (Fig. 3.6c and the left panel of Table 3.4) or other gyral regions (next section). Instead, sulcal regions mainly interact with locally connected neighboring gyral regions, which will be explained in details in the next section.

Table 3.5. Gyral-Sulcal Structural/Functional Connectivity in Dataset 1.

Con / Sub	Functional Connectivity						Structural Connectivity					
	LPCG LCS	LCS LPOG	LPOG LPOS	RPCG RCS	RCS RPOG	RPOG RPOS	LPCG LCS	LCS LPOG	LPOG LPOS	RPCG RCS	RCS RPOG	RPOG RPOS
1	1.18	1.00	1.20	0.93	1.11	0.92	0.99	0.49	0.99	0.99	0.66	0.16
2	1.12	0.96	1.08	1.16	1.17	0.80	0.37	0.37	0.19	0.19	0.93	0.00
3	1.22	1.30	1.13	1.03	1.15	0.78	0.12	0.12	0.00	0.24	0.12	0.12
4	1.19	1.19	0.73	1.22	1.26	0.81	0.38	1.89	0.00	0.00	0.00	0.38
5	0.66	0.96	1.08	1.04	1.45	1.47	1.31	0.88	0.88	0.44	3.94	0.00
6	0.84	1.05	1.38	1.02	0.92	0.61	0.85	1.70	0.00	1.70	2.55	0.00
7	0.78	0.76	1.39	0.67	1.07	1.22	0.62	0.00	0.31	0.00	0.31	0.00
8	1.28	0.90	0.66	0.99	1.20	0.99	1.04	0.35	0.69	0.35	1.04	0.00
9	1.28	1.18	0.90	1.07	1.20	0.84	1.56	0.39	0.00	0.00	0.00	0.00
10	0.89	0.96	0.78	1.30	1.43	1.14	0.11	0.16	0.90	0.90	0.26	0.16
11	0.97	1.05	0.70	1.23	1.26	1.38	0.73	0.46	0.46	0.27	0.27	1.46
Mean	1.04	1.03	1.00	1.06	**1.20**	0.99	0.73	0.62	0.40	0.46	0.92	0.21
Stdev	0.22	0.15	0.27	0.17	0.15	0.27	0.47	0.63	0.40	0.53	1.24	0.43
p-val	0.59	0.54	0.97	0.26	**0.00**	0.95	0.95	0.96	1.00	1.00	0.59	1.00

Structural/functional connectivity between adjacent gyri and sulci

The structural and functional connection patterns between adjacent gyri and sulci are shown in Fig. 3.6d. We can see that there are moderate functional connections between sulcal regions and their neighboring gyral regions (solid yellow lines in Fig. 3.6d) in spite of the very weak structural connections (dashed cyan curves in Fig. 3.6d) that can be revealed by in-vivo DTI data. However, a large number of neuroscience literature publications have demonstrated the inter-column cortico-cortical axonal connections within neighboring cortical regions [5, 30] that cannot be revealed by in-vivo DTI at the current stage, and these inter-column connections may explain the moderate functional connections between neighboring sulcal and gyral regions in Fig. 3.6d. The quantitative measurements of the structural and functional connection strengths between adjacent gyri and sulci shown in Fig. 3.6d are provided in Table 3.5. It is evident that the structural connections between adjacent gyri and sulci pairs are very weak, in comparison with the structural connection strengths between gyri pairs in Table 3.3. In contrast, the functional connection strengths between adjacent gyri and sulci are moderate, which are in-between the functional connection strengths between gyrus-gyrus pairs (Table 3.3) and those between sulcus-sulcus pairs (Table 3.4).

The results in Fig. 3.6c-d and Table 3.3-Table 3.5 have demonstrated two major points about structural and functional connectivity of cortical sulci: 1) both structural and functional connection strengths between sulci and other remote cortical regions (except the RCS-LCS pair) are relatively weak; 2) sulcal regions mainly interact directly with their neighboring gyri, and at the same time, they communicate indirectly with other remote gyral/sulcal regions via their neighboring gyri hubs. Also, we interpret that the moderate functional connectivity between adjacent sulci and gyri has its structural underpinnings. That is, the inter-column cortico-cortical axonal projections that cannot be revealed by DTI data. Therefore, these results further support our hypothesized functional model of cortical gyri and sulci: gyri are the global functional integration hubs, and sulci are the local functional units.

Replicative study on superior temporal regions

In addition to the PCG, POG, CS, and PCS examined in previous sections, a replicative study was conducted on the superior temporal gyrus/sulcus. Specifically, we extracted landmarks on both superior temporal gyrus (STG) and superior temporal sulcus (STS) in Dataset 1 via the same approaches and performed similar analyses, except that we used the corresponding individual mean and variance obtain from previous studies when normalizing FC values to enable a fair comparison. The results are shown in Table 3.6. Though the functional connectivity level is relatively lower in the superior temporal regions than those previously studied in the pre-central and post-central areas, it is still evident that the gyrus-gyrus functional connectivity (average: 0.99) is significantly stronger than the sulcus-sulcus connectivity (average: 0.64) (p-value=0.004), while adjacent gyrus-sulcus connectivity (0.79 for the left hemisphere and 0.72 for the right hemisphere) is moderate and in-between. Although no structural fiber connections between any pair of STG and STS were revealed by DTI (Table SOMETHING), the fibers connecting STGs to other cortical areas are abundant, indicating possible indirect connections between left and right STGs. The above findings are in line with our aforementioned results in the pre-central and post-central cortical areas, suggesting that the proposed functional model of cortical gyri and sulci can be replicated in other cortical regions such as left and right STG and STS.

Table 3.6. STRUCTURAL/FUNCTIONAL CONNECTIVITY OF SUPERIOR TEMPORAL REGIONS.

Con Sub	Functional Connectivity				Structural Connectivity			
	LSTG RSTG	LSTS RSTS	LSTG LSTS	RSTG RSTS	LSTG RSTG	LSTS RSTS	LSTG LTST	RSTG RSTS
1	1.00	1.10	0.79	0.76	0	0	0	0
2	1.01	0.61	0.78	0.68	0	0	0	0
3	0.55	0.21	0.67	0.41	0	0	0	0
4	0.90	0.88	0.88	0.81	0	0	0	0
5	0.99	0.56	1.01	0.92	0	0	0	0
6	N/A	N/A	N/A	N/A	N/A	N/A	N/A	N/A
7	0.68	0.48	0.38	0.53	0	0	0	0
8	1.22	0.33	0.86	0.43	0	0	0	0
9	1.36	0.91	1.31	1.13	0	0	0	0
10	0.89	0.64	0.51	0.36	0	0	0	0
11	1.28	0.63	0.71	1.17	0	0	0	0
Mean	**0.99**	**0.64**	**0.79**	**0.72**	0	0	0	0
Stdev	0.25	0.27	0.26	0.29	N/A	N/A	N/A	N/A

Two-sample statistical significance test without equal variance assumption			
Test	LSTG-RSTG>LSTS-RSTS	LSTG-RSTG>LSTG-LSTS	LSTG-RSTG>RSTG-RSTS
p-value	**0.004**	**0.05**	**0.02**

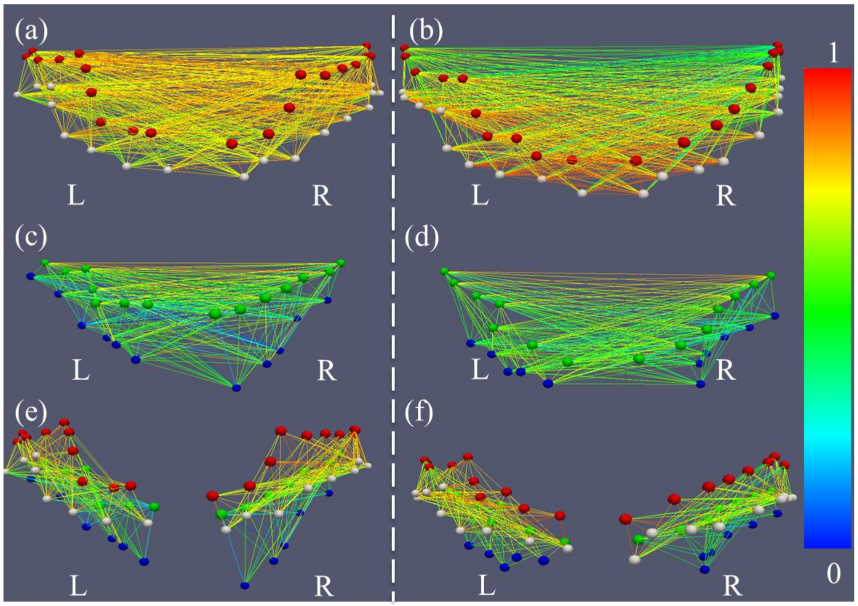

Fig. 3.7. Examples of functional connectivity patterns for two randomly selected subjects (left and right panels, respectively). Red, white, green, and blue bubbles represent the landmarks on PCG, POG, CS, and POS, respectively. The edges are colored based on the functional connectivity strength (without individualized normalization) according to the color bar on the right. (a) and (b) are gyrus-gyrus pairs; (c) and (d) are sulcus-sulcus pairs; (e) and (f) are adjacent gyrus-sulcus pairs.

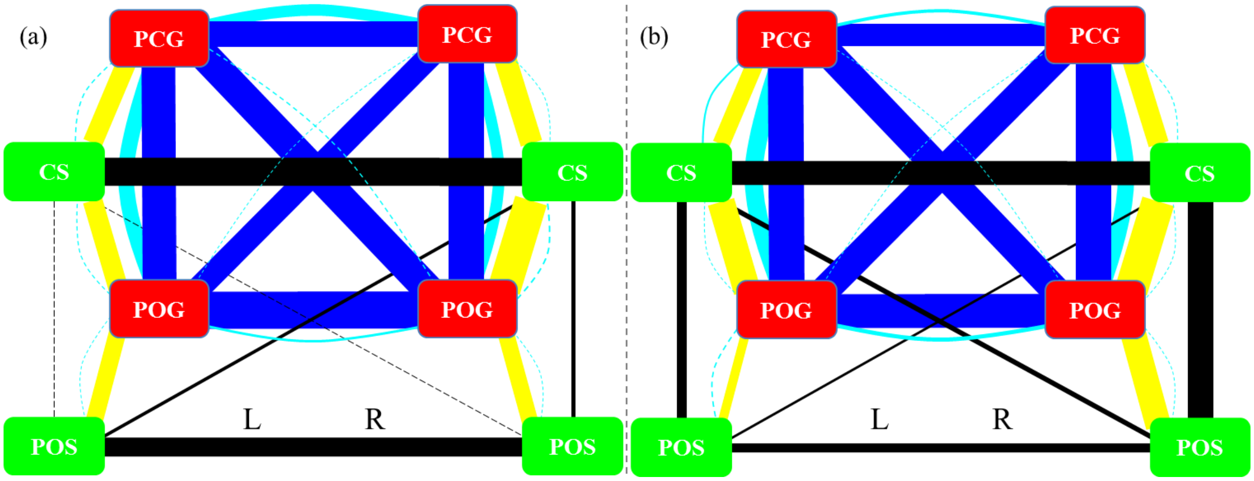

Fig. 3.8. Overall joint representation of structural/functional connectivity of gyri and sulci. Edges colored in cyan represent structural connections, and those colored in blue, black, and yellow represent functional connections for gyrus-gyrus, sulcus-sulcus, and gyrus-sulcus patterns, respectively. (a) Dataset 1. (b) The replication of the overall joint representation of structural and functional connectivity of gyri and sulci in the second dataset.

Overall structural/functional connectivity among gyri and sulci

To provide an illustrative overview of the results discussed so far, Fig. 3.7 shows two examples of the functional connectivity patterns between the landmarks on gyrus-gyrus, sulcus-sulcus, and adjacent gyri-sulci pairs. It is apparent that the gyrus-gyrus functional connections (Fig. 3.7a, b), sulcus-sulcus functional connections (Fig. 3.7c, d), and adjacent gyri-sulci functional connections (Fig. 3.7e, f) are strong, weak, and moderate, respectively. This visualization illustrates the major findings in previous sections. Also, the sub-figures in Fig. 3.6b-d are integrated and summarized in Fig. 3.8a, that is, all of the structural/functional connection patterns are represented by the colored curves/lines in Fig. 3.8a. Based on the visualizations in Fig. 3.8a, it becomes even more evident that gyri (red boxes in Fig. 3.8a) are the functional integration hubs, while the sulci serve as the local functional units. Quantitatively, we measured the graph edge degrees of the functional connection networks for all of the gyri and sulci, as shown in Table 3.7. The graph degrees are normalized to [0, 1], where 0 means no connection at all and 1 means the corresponding landmark connects to all possible nodes. It is evident that the graph edge degrees of the gyri nodes are significantly higher than those of the sulci nodes (overall p-value=1.90E-30, two-sample, right-tailed test without equal variance assumption). In addition, the averaged total functional connection strengths of the gyri nodes are significantly higher than those of sulci (p-value=0.004). Altogether, the quantitative results in this section further support our hypothesis: gyri are the global functional integration hubs and sulci are the local functional units.

Table 3.7. AVERAGE GRAPH EDGE DEGREES OF DATASET 1[ii].

Gyri	Mean	Stdev	Sulci	Mean	Stdev
LPCG	0.66	0.20	LCS	0.50	0.18
LPOG	0.65	0.17	LPOS	0.43	0.21
RPCG	0.65	0.19	RCS	0.55	0.15
RPOG	0.68	0.15	RPOS	0.41	0.22

[ii] Threshold=1. The degree values are normalized to [0, 1] where 0 means no connection at all and 1 means the corresponding node connects to all possible nodes. The same parameters apply to subsequent tables of graph edge degrees.

Table 3.8. GYRAL STRUCTURAL/FUNCTIONAL CONNECTIVITY IN DATASET 2.

Con / Sub	Functional Connectivity						Structural Connectivity					
	RPCG LPCG	RPOG LPCG	LPOG LPCG	RPCG LPOG	RPCG RPOG	RPOG LPOG	RPCG LPCG	RPOG LPCG	LPOG LPCG	RPCG LPOG	RPCG RPOG	RPOG LPOG
1	1.11	1.27	1.21	1.25	1.54	1.39	0.50	0.00	8.00	1.21	6.86	7.93
2	1.26	1.15	1.21	1.05	1.17	1.10	0.00	0.62	3.11	0.00	17.73	0.00
3	1.20	1.18	1.38	1.24	1.19	1.27	1.69	0.08	11.69	0.00	7.08	2.85
4	0.92	1.11	1.44	1.05	0.97	0.85	6.34	0.27	8.99	0.00	6.82	4.12
5	0.80	1.06	1.13	1.07	1.27	1.19	3.58	0.00	9.69	0.65	10.01	1.38
6	1.15	0.99	1.02	1.30	1.31	1.36	0.00	0.00	16.75	0.00	9.44	0.05
7	0.82	1.33	1.21	0.91	1.01	1.37	1.75	0.00	12.29	0.00	10.86	0.00
8	1.24	1.09	1.30	1.35	1.16	1.19	0.13	0.00	14.46	0.00	8.41	2.10
Mean	1.06	**1.15**	**1.24**	**1.15**	**1.20**	**1.22**	**1.75**	0.12	**10.62**	0.23	**9.65**	2.30
Stdev	0.19	0.11	0.13	0.15	0.18	0.18	2.23	0.22	4.19	0.46	3.60	2.72
p-val	0.38	**0.01**	**0.00**	**0.03**	**0.01**	**0.01**	0.19	1.00	**0.00**	1.00	**0.00**	0.11

Table 3.9. SULCAL STRUCTURAL/FUNCTIONAL CONNECTIVITY IN DATASET 2.

Con / Sub	Functional Connectivity						Structural Connectivity					
	RCS LCS	RPOS LCS	LCS LPOS	RCS LPOS	RCS RPOS	RPOS LPOS	RCS LCS	RPOS LCS	LCS LPOS	RCS LPOS	RCS RPOS	RPOS LPOS
1	1.13	0.82	0.63	0.65	0.86	1.01	0.00	0.00	0.00	0.00	0.00	0.00
2	0.91	0.94	0.84	0.73	1.71	0.90	0.00	0.00	0.00	0.00	0.00	0.00
3	1.06	0.77	0.80	0.55	0.95	0.62	0.00	0.00	0.00	0.00	0.00	0.00
4	1.22	1.07	0.87	0.73	1.43	0.76	0.00	0.00	0.00	0.00	0.00	0.00
5	1.24	0.84	1.37	0.97	1.06	1.04	0.00	0.00	0.00	0.05	0.00	0.00
6	0.98	0.92	1.04	1.08	1.18	1.22	0.00	0.00	0.00	0.00	0.00	0.00
7	1.14	0.88	0.92	0.74	0.97	0.69	0.00	0.00	0.00	0.00	0.00	0.00
8	1.05	0.51	0.76	1.05	0.66	0.88	0.00	0.00	0.00	0.00	0.00	0.00
Mean	**1.09**	**0.84**	0.90	**0.81**	1.10	0.89	**0.00**	**0.00**	**0.00**	**0.00**	**0.00**	**0.00**
Stdev	0.12	0.16	0.22	0.20	0.33	0.20	0.00	0.00	0.00	0.00	0.00	0.00
p-val	**0.06**	**0.03**	0.26	**0.03**	0.41	0.17	N/A	N/A	N/A	N/A	N/A	N/A

Table 3.10. GYRAL-SULCAL STRUCTURAL/FUNCTIONAL CONNECTIVITY IN DATASET 2.

Con Sub	Functional Connectivity						Structural Connectivity					
	LPCG LCS	LCS LPOG	LPOG LPOS	RPCG RCS	RCS RPOG	RPOG RPOS	LPCG LCS	LCS LPOG	LPOG LPOS	RPCG RCS	RCS RPOG	RPOG RPOS
1	1.07	1.18	0.76	1.13	1.16	0.94	3.07	0.00	0.21	0.07	0.14	0.00
2	0.88	1.01	0.94	1.08	1.36	1.31	0.00	0.93	1.24	2.49	1.87	0.00
3	1.07	1.10	0.63	1.26	1.24	0.90	2.69	0.77	0.08	0.31	0.15	0.62
4	1.14	1.13	0.87	1.08	1.31	1.31	0.05	0.11	0.49	0.05	0.43	0.27
5	0.85	1.41	1.02	0.90	0.82	1.17	0.24	0.08	2.12	0.24	0.00	0.00
6	0.87	1.15	0.96	0.76	1.13	1.19	0.71	0.11	0.05	0.16	0.38	0.33
7	1.08	1.06	0.86	0.80	1.39	1.32	0.58	0.13	1.68	0.39	0.19	0.00
8	1.08	0.99	1.08	1.33	1.22	0.77	0.92	0.39	0.66	0.79	0.13	0.00
Mean	1.00	**1.13**	0.89	1.04	**1.20**	1.11	1.03	0.32	0.82	0.56	0.41	0.15
Stdev	0.12	0.13	0.14	0.21	0.18	0.22	1.19	0.35	0.78	0.81	0.60	0.23
p-val	0.91	**0.03**	0.07	0.57	**0.01**	0.18	0.47	1.00	0.74	0.91	0.99	1.00

Table 3.11. AVERAGE GRAPH EDGE DEGREES OF DATASET 2.

Gyri	Mean	Stdev	Sulci	Mean	Stdev
LPCG	0.61	0.07	LCS	0.51	0.06
LPOG	0.62	0.05	LPOS	0.43	0.11
RPCG	0.63	0.11	RCS	0.57	0.05
RPOG	0.64	0.08	RPOS	0.49	0.13

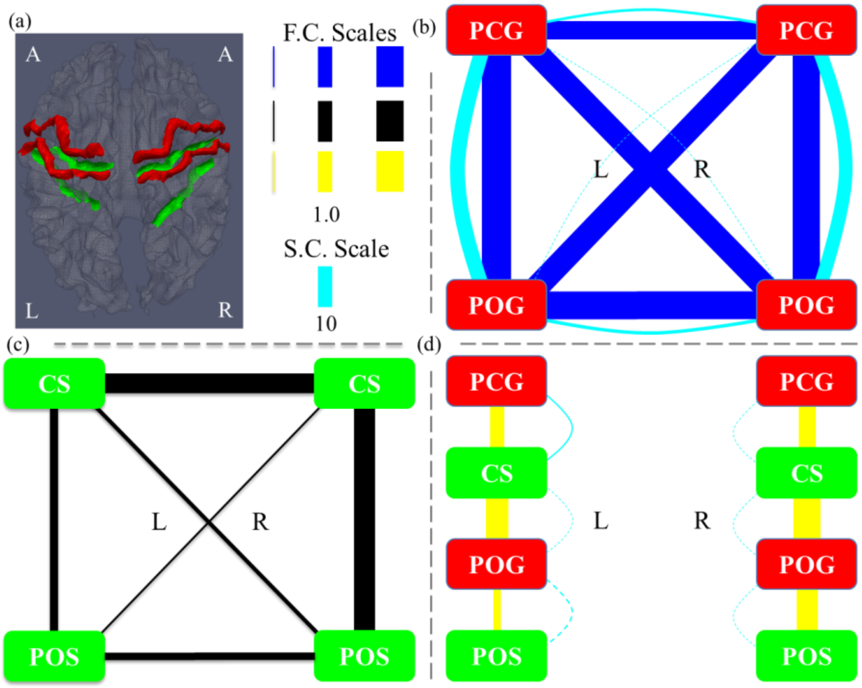

Fig. 3.9. Results of dataset 2 (in correspondence with Fig. 3.6). (a) Illustration of the four gyral regions (red) and four sulcal regions (green). In (b)-(c), the width of a functional edge (blue, black, and yellow) is linear with regard to the functional connectivity (F.C.); that of a structural edge (cyan) is proportional to the structural connectivity (S.C.). The right panel shows: (1) the size of functional connection edges with 80% of, 100% of, and 120% of average functional connectivity, respectively; and (2) the structural connection edges with ten times of the average number of fibers connecting a pair of cortical landmarks (structural connectivity value of 10.0). Weak edges (width less than one) are shown in dashed lines. (b) Joint representation of structural and functional connectivity among four gyri. Strong direct DTI-derived structural connectivity was observed in the LPCG-LPOG, RPCG-RPOG, LPCG-RPCG, and LPOG-RPOG pairs. (c) Joint representation of structural and functional connectivity among four sulci. Strong structural connectivity was not observed from data. (d) Joint representation of structural and functional connectivity between adjacent gyrus and sulcus. Weak direct structural connectivity was observed from the DTI data.

Reproducibility study on dataset 2

All experiments and results for dataset 1 are repeated for dataset 2. Specifically, Table 3.8-Table 3.10 correspond to Table 3.3-Table 3.5 in the main text; Table 3.11 corresponds to Table 3.7; Fig. 3.9 corresponds to Fig. 3.6.

The structural and functional connection patterns among four gyri in dataset 2 are shown in Fig. 3.9b. Similar to the results in dataset 1 (Fig. 3.6b), both strong structural (cyan curves) and functional (blue lines) connections exist in gyrus-gyrus pair. Specifically, strong structural connections were observed in the PCG-POG pair of both hemispheres; moderate structural connections were observed between the RPCG-LPCG pair, as well as the RPOG-LPOG pair. Although in dataset 2 the RPCG-LPCG structural connection is only moderate in comparison with the strong structural connection of the RPCG-LPCG pair in dataset 1, the difference is minor and they are both above average (1.0) as shown in Table 3.8 (dataset 2) and Table 3.3 (dataset 1, main text). The strong functional connectivity patterns are very consistent with the findings in dataset 1, suggesting the reproducibility of the conclusions drawn from the results in dataset 1.

The structural and functional connection patterns among four sulci in dataset 2 are shown in Fig. 3.9c. Despite the difference in the RCS-RPOS pair where dataset 2 exhibits stronger functional connectivity while dataset 1 does not, the overall connection patterns are quite consistent. For instances, the functional connections between those sulci pairs of RPOS-LCS, LCS-LPOS, RCS-LPOS, and RCS-RPOS are week (black lines in Fig. 3.9c). And both of RCS-LCS and RPOS-LPOS pairs show strong functional connectivity. Similar to that in dataset 1, no direct DTI-derived structural connections between sulci were found, as shown in Table 3.9.

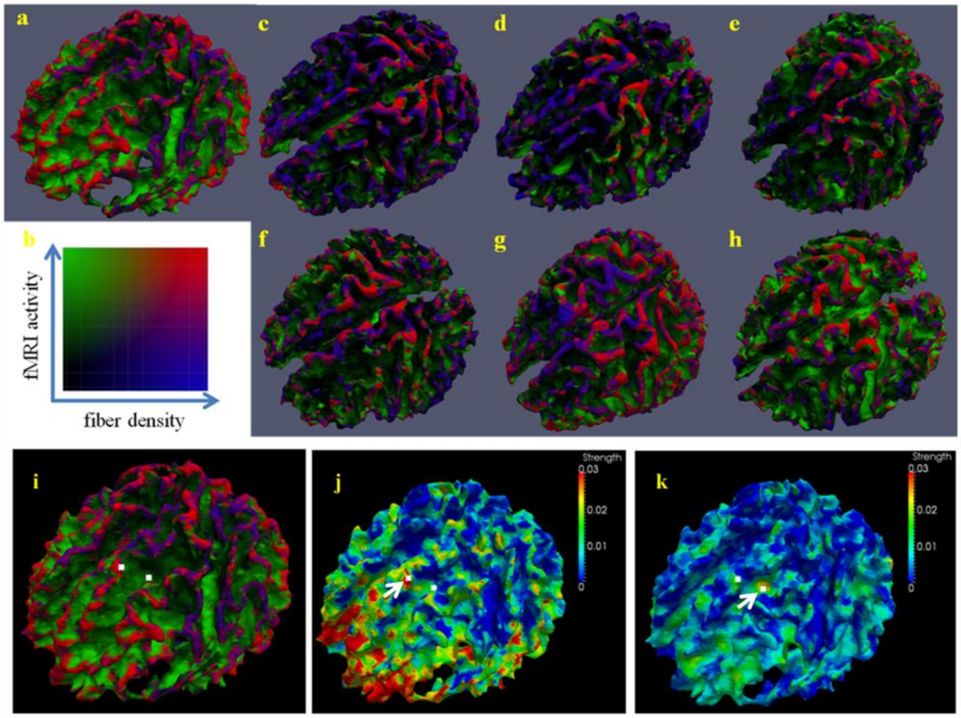

Fig. 3.10. Functional activities on gyri and sulci revealed by R-fMRI. (a): Joint visualization of R-fMRI activity and fiber density on cortical surface. The color map is in (b), in which red means region with both high fiber density and fMRI activity, while black represents region with both low fiber density and fMRI activity. It is apparent that most red regions are located on gyri, while most black regions are on sulci. The average spectral power in gyral regions is 1.5 times that in sulcal regions. (c)-(h): six additional cases of (a). (i): Two randomly picked voxels from the gyral and sulcal regions in the same subject in (a). The two voxels are represented by the white boxes. (j): Functional interaction strength between the voxel on gyral region (highlighted by the white arrow) and all other voxels on the cortical surface. The color bar is on the right. Red and blue represent strong and weak interaction, respectively. It is evident that the gyral voxel has significant long-distance functional interactions with other cortical voxels. (k): Functional interaction strength between the voxel on sulcal region (highlighted by the white arrow) and all other voxels on the cortical surface. The color bar is on the right. Red and blue represent strong and weak interaction, respectively. It is evident that the picked sulcal voxel has much less long-distance functional interactions with other cortical voxels, in comparison with the picked gyral voxel.

Fig. 3.9d shows the structural and functional connection patterns between adjacent gyri and sulci. In conjunction with the quantitative results in Table 3.10, it is evident that the structural and functional patterns among by adjacent gyri and sulci in dataset 2 are very consistent with the results from dataset 1. For instances, adjacent gyrus-sulcus pair shows moderate functional connectivity, while the direct DTI-derived structural connectivity is weak. In comparison with gyri pairs, the functional connectivity between an adjacent gyrus-sulcus pair is weaker, which might be due to the lack of direct structural connections. In comparison with sulci pairs, however, the functional connectivity of adjacent gyrus-sulcus pair is stronger as of the local connections formed by inter-column cortico-cortical connections.

Reproducibility study via whole brain analysis

In addition to the quantitative analysis of structural/functional connection patterns of four gyri and sulci, we examined the functional activities on the gyral and sulcal regions in the whole cerebral cortex. Specifically, the R-fMRI signal spectrum energy (indicator of brain activity, [2]) was mapped on gyral and sulcal regions (Fig. 3.10a-h), on which axonal fiber densities [26] are also quantitatively measured. On average among eleven subjects, the spectral power in gyral regions is 1.5 times of that in sulcal regions, suggesting that gyral regions are substantially more active than sulcal regions. In particular, most of the highest spectrum power regions are co-localized with high fiber densities on the gyral crests, as represented by the red regions in Fig. 3.10a-h. These whole-brain analysis results are consistent with our previous reports [26] and agree with our findings in the above sections, further supporting our hypothesized functional model of cortical gyri and sulci.

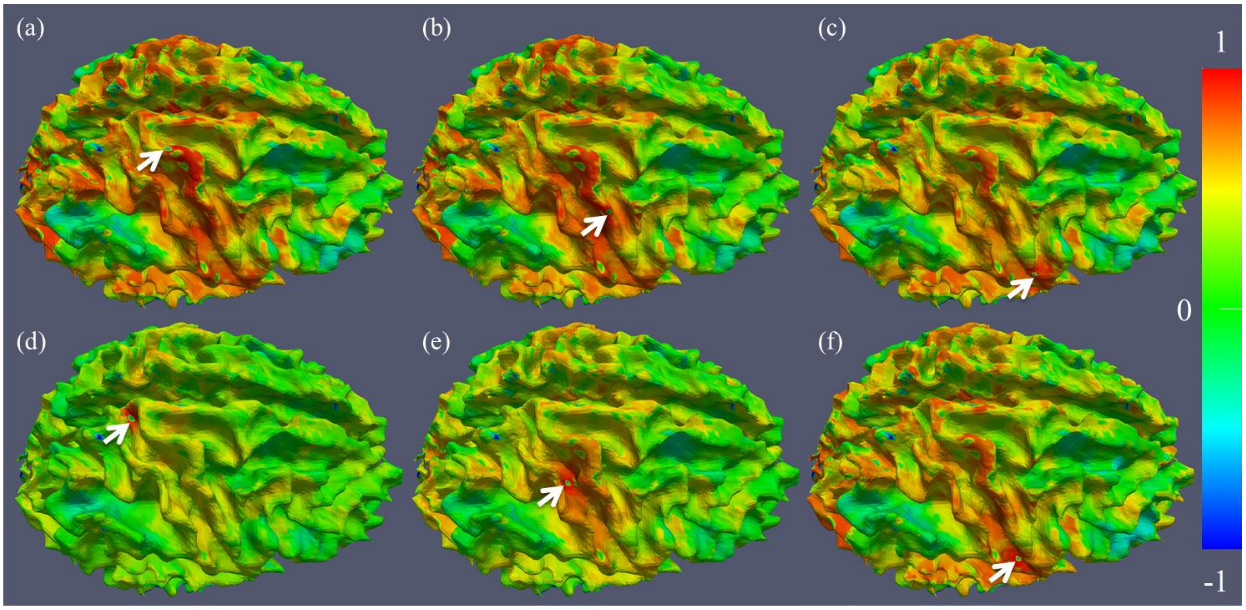

Fig. 3.11. Examples of cortical connectivity maps of selected landmarks (pointed by white arrows). (a)-(c): three landmarks from the RPCG; (d)-(f): three landmarks from the RCS. The color bar is on the right. The results shown in this figure are in agreement with the proposed functional model.

To further illustrate the above finding, we randomly picked two voxels in the gyral and sulcal regions shown in Fig. 3.10i. Then, we measured the functional interaction strength between other cortical voxels and the picked voxels in consideration as follows. A time-frequency map (akin to the methods in [83]) generated from Wavelet transform is converted into a binary interaction map using statistical significance test, in which elements with statistical significant power are valued one. The interaction strength is derived from the interaction map by counting the number of one-elements outside the Cone-Of-Influence (COI) [83]. The ratio of this number and the total number of elements outside the COI is defined as the interaction strength, which can be regarded as a measurement of how strongly two R-fMRI time series interacts in the time-frequency domain. The rationale of using Wavelet transform in this experiment is that Wavelet transform reveals fine correlation structure between time series that Pearson Correlation could not. After that, we mapped the functional interaction strength onto the cortical surface, as shown in Fig. 3.10j and Fig. 3.10k. It is evident that the gyral voxel has much more long-distance functional interactions (Fig. 3.10j) than the sulcal voxel (Fig. 3.10k), consistent with our hypothesis that there are many more long-distance functional interactions on gyral regions than sulcal region. Additional examples using Pearson correlation for randomly selected cortical landmarks are shown in Fig. 3.11, which further replicates the findings in Fig. 3.10j-k.

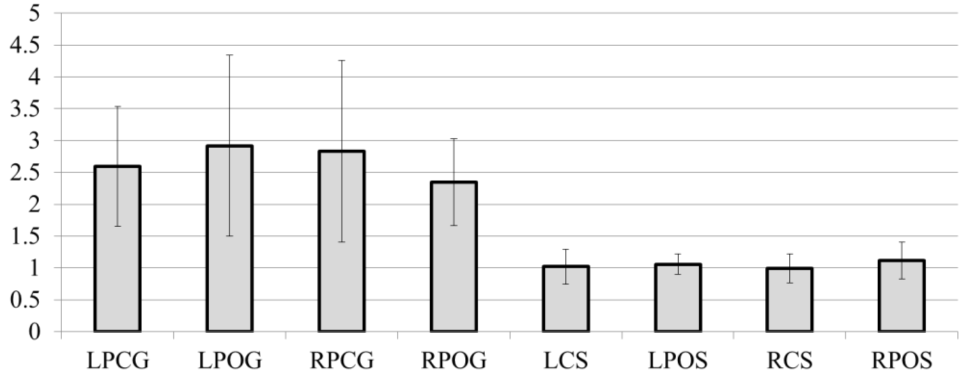

Fig. 3.12. Ratio of the number of gyral voxels over that of sulcal voxels within the top 1% of the most functionally connected cortical voxels in the first dataset.

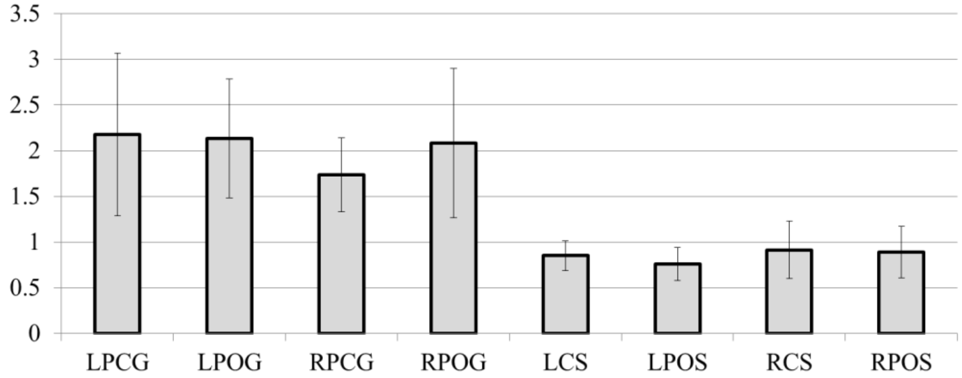

Fig. 3.13. Ratio of the number of gyral voxels over that of sulcal voxels within the top 1% of the most functionally connected cortical voxels in the second dataset.

In addition to the above individual voxel-wise analysis, a whole-brain functional connectivity analysis was performed for all of the cortical landmarks in the two datasets. Specifically, the functional correlation strengths between the aforementioned landmarks and other cortical voxels in the whole brain were measured. From the top 1% of the most correlated cortical landmark/voxel pairs, we collected the ratios of the number of gyral voxels over that of sulcal voxels. On average, for those strongly connected cortical voxels on gyral regions (LPCG, LPOG, RPCG, and RPOG), 72.76% of the cortical voxels on the other ends of these connections are located on gyri and only 27.24% of them are located on sulci (a ratio of 2.67). As a comparison, for those strongly connected cortical voxels on sulcal regions (LCS, LPOS, RCS, and RPOS), 51.14% of the cortical voxels on the other ends of these connections are on located on gyri and 48.86% of them are located on sulci (a ratio of 1.05). These ratio differences are summarized in Fig. 3.12 and Fig. 3.13 for both datasets. These results suggest that a majority of the strong functional connections to gyral regions originate from gyri too. This whole-brain analysis result further supports our functional model of cortical gyri and sulci: gyri are the functional integration hubs.

CHAPTER 4

CONCLUSION

The latest functional brain imaging techniques offer unparalleled opportunities for researchers to extend our understanding of the human brain into a deeper level. This thesis presents our efforts in discovering the functional interactions in the human brain using fMRI from both signal processing and neuroscience perspectives.

Our contributions of the signal processing part are summarized in the following five aspects. (1) EMCD extracts and uses the mean curve as the useful signal while the residue signal is used in subsequent signal decompositions. In short, EMCD extracts coarser-to-finer scale signals, reducing the error accumulation against useful low-frequency components. (2) A scale control algorithm was designed and implemented to deal with the instability as of the sparse distribution of extrema causing problems in interpolating and recovering superior and inferior envelopes, thus improving the accuracy and reliability of the decomposition procedure. In addition, this algorithm makes it possible to moderately control the scale at which the extracted component will be, which is helpful when some prior knowledge of the intrinsic signal composition is present. (3) The low-frequency mean curves extracted by EMCD, instead of high-frequency IMFs by EMD, are what we need to reconstruct in fMRI. For instance, in resting state fMRI analysis, we aim to reconstruct the neuronal oscillation signals in the range of 0.01Hz to 0.1Hz [2, 17], which is in the low-frequency bands. Therefore, the mean curve extraction in the proposed EMCD method fulfills the requirements of resting state fMRI time series analysis, while the IMFs from EMD do not. (4) We successfully applied EMCD in processing and analyzing fMRI time series data, including resting state fMRI [17, 50], task-based fMRI [52, 56], and natural stimulus fMRI [54]. (5) The EMCD framework has been extensively evaluated and validated by synthesized signals, independent diffusion tensor imaging (DTI) data, comparison with other methods, and verification by neuroscience domain knowledge.

For the data analysis part, we presented two lines of experimental and computational studies to formally propose a hypothesized functional model of gyri and sulci. First, we defined a series of cortical landmarks on both gyri and sulci, and analyzed the structural and functional connectivity among these gyral and sulcal landmarks. In particular, we assessed the functional connectivity patterns among gyral-gyral, gyral-sulcal and sulcal-sulcal landmark pairs over all of the eight selected functional areas. Second, we performed whole brain voxel-wise analyses to measure the strengths of functional activities and functional connections on gyral and sulcal regions. To examine the reproducibility of our studies, two independent multimodal DTI/R-fMRI datasets were used to examine the above hypothesized functional model. Collectively, these studies and the experimental results have supported a common functional model based on the common structural brain architecture: gyri are the global functional integration hubs and sulci are the local functional units.

Conceptually, the studies of the fundamental functional mechanism of cortical gyri and sulci in our study are rooted in the following two methodological considerations. First, DTI is a prominent imaging technique that can quantitatively map axonal fiber connections in vivo [16]. Our DTI studies [26] have revealed that axonal fiber wiring patterns closely follow cortical gyral folding pattern and fiber terminations concentrate on gyri. This finding provides a solid structural basis for the proposed functional model of the brain, that is, gyri are the functional integration hubs in that axonal fibers are the structural substrates of functional integration of the brain.

Second, R-fMRI is a powerful functional neuroimaging technique that can reveal the functional architecture of the brain [17]. In particular, multimodal DTI and R-fMRI data has the promise of elucidating the common structural and functional brain architectures and their relationships. In addition to the investigation of the proposed functional model of cortical gyri and sulci via multimodal DTI/R-fMRI data, this work also revealed that structural connections, either direct or indirect, are the structural underpinnings of functional connectivity. Altogether, the studies explicitly explained the close relationships between structural and functional connectivity.

At the current stage, we only used the landmarks from four major gyri/sulci in the primary motor and primary somatosensory systems for the study of the proposed functional model of gyri and sulci. This work can be naturally extended and enhanced by including landmarks from other major gyri and sulci in the cerebral cortex in the future, which entails larger scale of manual segmentation and labeling of cortical structures in a large-scale dataset. Also, in this work, the cortical landmarks on gyri and sulci do not possess structural and functional correspondences across individuals. In the future, we plan to use our recently developed cortical landmark optimization approaches [23, 52] to define and optimize these cortical landmarks so that they will have correspondences in different brains. In this case, their structural and functional connectivity patterns can be integrated and compared across populations, which could potentially provide additional supporting evidence to the proposed functional model of gyri and sulci.

Finally, we envision that the proposed functional model and its supporting experiment results could provide a foundation for future elucidation of fine-scale functional mechanisms of the cerebral cortex, for instance, how the gyri and sulci functionally interact with subcortical regions in resting state [17], during task performance [3], or under natural stimulus of movie watching [54, 62]. The verified functional model and its associated computational approaches could possibly enable and facilitate many novel studies and applications in neuroimaging, cognitive neuroscience, and clinical neuroscience. For instances, the differentiation of the functional roles of gyri and sulci can help achieve better localization and selection of brain regions in different functional neuroimaging and cognitive neuroscience studies, and the functional interactions among gyral-gyral, gyral-sulcal, and sulcal-sulcal landmarks could be used to elucidate the potential dysfunctions in neurological or psychiatric diseases/conditions.

REFERENCES

1. Heeger, D.J. and D. Ress, *What does fMRI tell us about neuronal activity?* Nat Rev Neurosci, 2002. **3**(2): p. 142-151.
2. Buzsaki, G. and A. Draguhn, *Neuronal oscillations in cortical networks.* Science, 2004. **304**(5679): p. 1926-1929.
3. Logothetis, N.K., *What we can do and what we cannot do with fMRI.* Nature, 2008. **453**(7197): p. 869-878.
4. Rakic, P., *Specification of cerebral cortical areas.* Science, 1988. **241**(4862): p. 170-176.
5. Kandel, E.R., J.H. Schwartz, and T.M. Jessell, *Principles of Neural Science*. 4th edition ed2000.
6. Passingham, R.E., K.E. Stephan, and R. Kötter, *The anatomical basis of functional localization in the cortex.* Nat Rev Neurosci, 2002. **3**(8): p. 606-616.
7. Rettmann, M.E., et al., *Automated sulcal segmentation using watersheds on the cortical surface.* Neuroimage, 2002. **15**(2): p. 329-344.
8. Zilles, K. and K. Amunts, *Centenary of Brodmann's map--conception and fate.* Nat Rev Neurosci, 2010. **11**(2): p. 139-145.
9. Liu, T., *A few thoughts on brain ROIs.* Brain Imaging Behav, 2011. **5**(3): p. 189-202.
10. Thirion, J.P. *Extremal mesh and the understanding of 3D surfaces*. in *IEEE Workshop on Biomedical Image Analysis*. 1994. Seattle, WA, USA: IEEE.
11. Fischl, B., M.I. Sereno, and A.M. Dale, *Cortical surface-based analysis. II: Inflation, flattening, and a surface-based coordinate system.* Neuroimage, 1999. **9**(2): p. 195-207.

12. Lohmann, G. and D.Y. von Cramon, *Automatic labelling of the human cortical surface using sulcal basins.* Med Image Anal, 2000. **4**(3): p. 179-188.

13. Shi, Y., et al., *Hamilton-Jacobi skeleton on cortical surfaces.* IEEE Trans Med Imaging, 2008. **27**(5): p. 664-673.

14. Li, G., et al. *Automatic cortical sulcal parcellation based on surface principal direction flow field tracking*. in *IPMI*. 2009. Williamsburg, VA, United states: Springer Verlag.

15. Li, G., et al., *An automated pipeline for cortical sulcal fundi extraction.* Med Image Anal, 2010. **14**(3): p. 343-359.

16. Mori, S. and J. Zhang, *Principles of diffusion tensor imaging and its applications to basic neuroscience research.* Neuron, 2006. **51**(5): p. 527-539.

17. Fox, M.D. and M.E. Raichle, *Spontaneous fluctuations in brain activity observed with functional magnetic resonance imaging.* Nat Rev Neurosci, 2007. **8**(9): p. 700-711.

18. Honey, C.J., et al., *Predicting human resting-state functional connectivity from structural connectivity.* Proc Natl Acad Sci, 2009. **106**(6): p. 2035-2040.

19. Zhang, T., et al., *Predicting functional cortical ROIs via DTI-derived fiber shape models.* Cereb Cortex, 2011.

20. Li, K., et al., *Individual functional ROI optimization via maximization of group-wise consistency of structural and functional profiles.* Neuroinformatics, 2012.

21. Vincent, J.L., et al., *Intrinsic functional architecture in the anaesthetized monkey brain.* Nature, 2007. **447**(7140): p. 83-86.

22. Rilling, J.K., et al., *The evolution of the arcuate fasciculus revealed with comparative DTI.* Nat Neurosci, 2008. **11**(4): p. 426-428.

23. Zhu, D., et al., *Discovering dense and consistent landmarks in the brain,* in *IPMI*2011. p. 97-110.

24. Ge, B., et al. *Resting state fMRI-guided fiber clustering*. in *MICCAI*. 2011. Toronto, ON, Canada: Springer Verlag.

25. Lv, J., et al., *Activated fibers: fiber-centered activation detection in task-based FMRI,* in *IPMI*2011. p. 574-587.

26. Nie, J., et al., *Axonal fiber terminations concentrate on gyri.* Cereb Cortex, 2011.

27. Chen, H., et al., *Coevolution of gyral folding and structural connection patterns in primate brains.* Cereb Cortex, 2012.

28. Tuch, D.S., et al., *High angular resolution diffusion imaging reveals intravoxel white matter fiber heterogeneity.* Magn Reson Med, 2002. **48**(4): p. 577-582.

29. Deng, F., et al., *A Functional Model of Cortical Gyri and Sulci.* Neuroimage, 2012, in submission.

30. Thomson, A.M. and C. Lamy, *Functional maps of neocortical local circuitry.* Front Neurosci, 2007. **1**(1): p. 19.

31. Friston, K.J., et al., *Statistical parametric maps in functional imaging: A general linear approach.* Hum Brain Mapp, 1994. **2**(4): p. 189-210.

32. Bullmore, E., et al., *Wavelets and statistical analysis of functional magnetic resonance images of the human brain.* Stat Methods Med Res, 2003. **12**(5): p. 375-399.

33. Shimizu, Y., et al., *Wavelet-based multifractal analysis of fMRI time series.* Neuroimage, 2004. **22**(3): p. 1195-1202.

34. Descombes, X., F. Kruggel, and D.Y. von Cramon, *fMRI signal restoration using a spatio-temporal Markov Random Field preserving transitions.* Neuroimage, 1998. **8**(4): p. 340-349.

35. Hartvig, N.V. and J.L. Jensen, *Spatial mixture modeling of fMRI data.* Hum Brain Mapp, 2000. **11**(4): p. 233-248.

36. Woolrich, M.W., et al., *Fully bayesian spatio-temporal modeling of fMRI data.* IEEE Trans Med Imaging, 2004. **23**(2): p. 213-231.

37. Luo, H. and S. Puthusserypady, *fMRI data analysis with nonstationary noise models: a Bayesian approach.* IEEE Trans Biomed Eng, 2007. **54**(9): p. 1621-1630.

38. Calhoun, V.D., et al., *A method for making group inferences from functional MRI data using independent component analysis.* Hum Brain Mapp, 2002. **16**(2): p. 131-131.

39. Calhoun, V.D., J.J. Pekar, and G.D. Pearlson, *Alcohol intoxication effects on simulated driving: exploring alcohol-dose effects on brain activation using functional MRI.* Neuropsychopharmacology, 2004. **29**(11): p. 2097-2017.

40. Deng, F., et al., *FMRI Signal Analysis Using Empirical Mean Curve Decomposition.* IEEE Trans Biomed Eng, 2012, conditionally accepted.

41. Huang, N.E., et al., *The empirical mode decomposition and the Hilbert spectrum for nonlinear and non-stationary time series analysis.* Proc Royal Soc London. Series A: Mathematical, Physical and Engineering Sciences, 1998. **454**(1971): p. 903-995.

42. Flandrin, P., G. Rilling, and P. Gonçalvés, *Empirical Mode Decomposition as a Filter Bank.* IEEE Signal Processing Letters, 2004. **11**(2): p. 112-114.

43. Huang, N.E. and Z. Wu, *A study of the characteristics of white noise using the empirical mode decomposition method.* Proceedings: Mathematics, Physical and Engineering Sciences, 2004. **460**(2046): p. 1597-1611.

44. Flandrin, P. and P. Gonçalvés, *Empirical Mode Decompositions as data-driven wavelet-like expansions.* Int J of Wavelets, Multiresolution and Information Processing, 2004. **2**(4): p. 477-496.

45. Liang, H., et al., *Empirical mode decomposition of field potentials from macaque V4 in visual spatial attention.* Biol Cybern, 2005. **92**(6): p. 380-392.

46. McKeown, M.J., R. Saab, and R. Abu-Gharbieh, *A Combined Independent Component Analysis (ICA)/ Empirical Mode Decomposition (EMD) Method to Infer Corticomuscular Coupling*, in *IEEE EMBS Conference on Neural Engineering*2005. p. 679-682.

47. Sweeney-Reed, C.M. and S.J. Nasuto, *A novel approach to the detection of synchronisation in EEG based on empirical mode decomposition.* J Comput Neurosci, 2007. **23**(1): p. 79-111.

48. Zheng, T., M. Cai, and T. Jiang, *A novel approach to activation detection in fMRI based on empirical mode decomposition.* J Integr Neurosci, 2010. **9**(4): p. 407-427.

49. McGonigle, D.J., M. Mirmehdi, and A.L. Malizia, *Empirical mode decomposition in data-driven fMRI analysis*, in *Workshop on Brain Decoding, ICPR*2010. p. 25-28.

50. Li, K., et al., *Cortical surface based identification of brain networks using high spatial resolution resting state FMRI data*, in *ISBI*2010, IEEE Press: Rotterdam, Netherlands. p. 656-659.

51. Lv, J., et al. *Fiber-centered analysis of brain connectivities using DTI and resting state fMRI data*. in *MICCAI*. 2010. Springer Berlin / Heidelberg.

52. Zhu, D., et al., *Optimization of functional brain ROIs via maximization of consistency of structural connectivity profiles.* Neuroimage, 2012. **59**(2): p. 1382-1393.

53. Zhu, D., et al., *DICCCOL: Dense Individualized and Common Connectivity-based Cortical Landmarks.* Cereb Cortex, 2012.

54. Hu, X., et al., *Bridging low-level features and high-level semantics via fMRI brain imaging for video classification*, in *ACM Multimedia*2010, ACM: Firenze, Italy. p. 451-460.

55. FEAT. Available from: http://fsl.fmrib.ox.ac.uk/fsl/feat5.

56. Faraco, C.C., et al., *Complex span tasks and hippocampal recruitment during working memory.* Neuroimage, 2011. **55**(2): p. 773-787.

57. S., A.F., P. O., and W. K., *Evaluation campaigns and TRECVid*, in *ACM International Workshop on Multimedia Information Retrieval*2006, ACM: Santa Barbara, California, USA. p. 321-330.

58. Harel, J., C. Koch, and P. Perona, *Graph-based visual saliency*, in *NIPS*2007, MIT Press. p. 545-552.

59. Fransson, P., *Spontaneous low-frequency BOLD signal fluctuations: an fMRI investigation of the resting-state default mode of brain function hypothesis.* Hum Brain Mapp, 2005. **26**(1): p. 15-29.

60. De Luca, M., et al., *fMRI resting state networks define distinct modes of long-distance interactions in the human brain.* Neuroimage, 2006. **29**(4): p. 1359-1367.

61. Damoiseaux, J.S., et al., *Consistent resting-state networks across healthy subjects.* Proc Natl Acad Sci, 2006. **103**(37): p. 13848-13853.

62. Hasson, U., R. Malach, and D.J. Heeger, *Reliability of cortical activity during natural stimulation.* Trends Cogn Sci, 2010. **14**(1): p. 40-48.

63. Hasson, U., et al., *Intersubject synchronization of cortical activity during natural vision.* Science, 2004. **303**(5664): p. 1634-1640.

64. Wandell, B.A., S.O. Dumoulin, and A.A. Brewer, *Visual field maps in human cortex.* Neuron, 2007. **56**(2): p. 366-383.

65. Brandt, T., et al., *Reciprocal inhibitory visual-vestibular interaction. Visual motion stimulation deactivates the parieto-insular vestibular cortex.* Brain, 1998. **121**(9): p. 1749-1758.

66. Kleinschmidt, A., et al., *Neural correlates of visual-motion perception as object- or self-motion.* Neuroimage, 2002. **16**(4): p. 873-882.

67. Dieterich, M., *Functional brain imaging: a window into the visuo-vestibular systems.* Curr Opin in Neurol, 2007. **20**(1): p. 12-18.

68. Goycoolea, M.V., et al., *Musical brains: a study of spontaneous and evoked musical sensations without external auditory stimuli.* Acta Otolaryngol, 2007. **127**(7): p. 711-721.

69. Wong, P.C., et al., *The role of the insular cortex in pitch pattern perception: the effect of linguistic contexts.* J Neurosci, 2004. **24**(41): p. 9153-9160.

70. Remedios, R., N.K. Logothetis, and C. Kayser, *An auditory region in the primate insular cortex responding preferentially to vocal communication sounds.* J Neurosci, 2009. **29**(4): p. 1034-1045.

71. Cohen, Y.E., B.E. Russ, and G.W. Gifford, *Auditory processing in the posterior parietal cortex.* Behav Cogn Neurosci Rev, 2005. **4**(3): p. 218-231.

72. Klostermann, E.C., P. Loui, and A.P. Shimamura, *Activation of right parietal cortex during memory retrieval of nonlinguistic auditory stimuli.* Cogn Affect Behav Neurosci, 2009. **9**(3): p. 242-248.

73. Andersson, J.L., S. Skare, and J. Ashburner, *How to correct susceptibility distortions in spin-echo echo-planar images: application to diffusion tensor imaging.* Neuroimage, 2003. **20**(2): p. 870-888.

74. Liu, T., et al., *Brain tissue segmentation based on DTI data.* Neuroimage, 2007. **38**(1): p. 114-123.

75. Yuan, Y., et al. *Assessing graph models for description of brain networks*. in *ISBI*. 2011. Chicago, IL, United states: IEEE Computer Society.

76. ParaView. Available from: http://www.paraview.org.

77. Li, K., et al., *Gyral folding pattern analysis via surface profiling.* Neuroimage, 2010. **52**(4): p. 1202-1214.

78. Nie, J., et al., *Reconstruction of central cortical surface from brain MRI images: method and application*, in *ISBI*2007. p. 213-216.

79. MedINRIA. Available from: http://www-sop.inria.fr/asclepios/software/MedINRIA.

80. NA-MIC. Available from: http://hdl.handle.net/1926/1687.

81. Deligianni, F., et al., *Inference of functional connectivity from direct and indirect structural brain connections*, in *ISBI*2011. p. 849-852.

82. Brett, M., I.S. Johnsrude, and A.M. Owen, *The problem of functional localization in the human brain.* Nat Rev Neurosci, 2002. **3**(3): p. 243-249.

83. Chang, C. and G.H. Glover, *Time-frequency dynamics of resting-state brain connectivity measured with fMRI.* Neuroimage, 2010. **50**(1): p. 81-81.